

Variational and numerical modelling strategies for cost-effective simulations of driven free-surface waves

Floriane Gidel¹, Yang Lu*, Onno Bokhove*, Mark A Kelmanson

School of Mathematics and Leeds Institute for Fluid Dynamics, University of Leeds, Leeds, LS2 9JT, United Kingdom

ARTICLE INFO

Article history:

ABSTRACT

A new, cost-effective and widely applicable tool is developed for simulating three-dimensional (3D) water-wave motion in the context of the maritime-engineering sector, with specific focus on the formation and analysis of extreme waves generated within in-house experimental wave tanks. The resulting “numerical wave tank” is able to emulate realistic sea states in which complex wave-wave or wave-beach interactions occur. After first transforming the time-dependent free surface and oscillatory wavemaker into a static rectilinear domain with fixed boundaries, a variational approach is used to derive weak formulations that lead to a non-autonomous space-discrete Hamiltonian system to which robust (stable and mass-conserving) temporal integrators are applied. Specifically, first-order symplectic-Euler and second-order Störmer-Verlet schemes are implemented in the finite-element environment “Firedrake”, and convincing validation of the new tool is demonstrated via a comparison of its numerical results with data post-processed from real wave-tank experiments at the Maritime Research Institute Netherlands (MARIN). Current and future extensions to industrial applications are discussed.

1. Introduction

The design of maritime structures that are able to resist extreme events, such as freak waves, is a crucial requirement in the assurance of the safety of ships and crew. Despite significant progress, there is still room for augmentation of current knowledge on the formation and dynamics of freak waves, as well as their impact on maritime structures, particularly with regard to quantifying aspects of maritime design practice. One way to improve quantification of extreme-wave threat is to generate such waves in experimental tanks, wherein wave-structure interactions can be measured and calibrated against defining parameters. The experimental reproduction of rogue waves has motivated

*Corresponding authors

e-mail: o.bokhove@leeds.ac.uk & mmyl@leeds.ac.uk (Onno Bokhove)

¹Currently at SOPHiA Genetics, Pessac, France

several studies in the last two decades. For example, rogue-wave generation has been achieved via temporal focussing, concerning waves with different wavelengths travelling at different speeds meeting in a target area, cf. [1, 2, 3], and through the generation of a so-called Peregrine breather [4, 5] as well as experimentally [6].

However, the reliability of such tests depends on the number of repeated measurements; design practice requires averaged calculations of wave force over a large sample of measurements in order to reduce uncertainty [7]. The high cost of experiments precludes the maritime industry from being able to provide a sufficient number of measurements, thereby limiting reliability of current data and, as a direct consequence, update of design practice. The aim of this work is therefore to provide a new, cost-effective simulation tool of water waves for use by the maritime industry both to generate and to study extreme waves in their in-house experimental wave tanks.

An essential step in the simulation of freak-wave impact on marine structures is to maximize the amplitude and the steepness of the waves by combining nonlinear and dispersion effects. We therefore consider a deep-water “numerical wave tank” in which nonlinear dispersive waves are driven by a vertical or piston wavemaker. As per the in-house experimental basins of the Maritime Research Institute Netherlands (MARIN), the wavemaker motion aims to emulate realistic sea states, including complicated wave-wave interactions. In order to assist in the design of experimental configurations at MARIN, the present numerical model is built to address several computational and industrial challenges. Though it is motivated by the challenges raised at MARIN, the methodology proposed herein is by no means limited to their specific problems; rather, it can be applied across a wide spectrum of more general wave-impact studies that arise across the broader maritime-engineering sector.

The modelling of water waves constitutes a nonlinear free-surface boundary value problem in which capturing the geometry of the free surface at the air-water interface is itself a complicated core issue, because it is an *a priori* unknown component of the boundary of the solution domain. One can use iterative adaptive-mesh methods, in the vertical, for following the evolving free-surface location (see for instance [8, 9, 10, 11, 12]). Instead, in section 2, we extend the method proposed by [13], which consists of transforming the time-dependent free surface into a fixed boundary; we essentially use one “mesh” element in the vertical with a high level of p -refinement through the use of polynomials. We apply the same transformation technique to the wavemaker boundary to solve the equations in a fully static computational domain.

In contrast to previous work [13], we use a variational approach in section 2 to derive weak formulations from Luke’s variational principle [14]. Although accurate simulations of two-dimensional potential-flow waves using this transformed variational approach have been obtained [15], we extend it to accommodate the above-mentioned industrial applications, i.e. the new extension must incorporate 3D wave effects in order to simulate multi-directional wave propagation and its concomitant effect on wave-wave or wave-structure interactions. Moreover, we have included wavemakers in our model to allow others, from industry and alternative sectors, to investigate wavemaker motions that, for design and testing, generate specific waves in a target area.

In section 3 we obtain, by means of a variational approach, a non-autonomous (wavemaker-driven) space-discrete Hamiltonian system to which robust temporal integrators are applied [16], thereby complying with three essential computational requirements: stability, conservation of mass and boundedness of overall energy oscillations. Subsequently, in section 3.2.1, the first-order symplectic Euler scheme is introduced along with the second-order Störmer-Verlet scheme; details of their efficient numerical implementation within the finite-element modelling environment “Firedrake” [17, 18, 19, 20, 21] (www.firedrakeproject.org) are presented in Appendix B to Appendix D. In addition, convergence tests are performed to verify the accuracy of the spatial and temporal discretization methods.

In section 4, a comparison between numerically predicted free surfaces and experimental ones measured at MARIN [22] shows that both temporal-integration schemes perform well in the simulation of extreme freak waves. A Fourier analysis of time series for both measurements and simulations confirms this observation. In section 5, we summarise the strategies and achievements of the presented numerical model, augmented by a detailed presentation of current and future extensions to industrial applications.

2. Variational nonlinear potential-flow model

Water waves are often described by the Laplace equation, for the velocity potential $\phi(x, y, z, t)$ as a function of horizontal coordinates x and y , vertical coordinate z and time t , augmented by two nonlinear boundary conditions (BCs): a kinematic BC, which expresses that the boundary moves with the fluid, and a dynamic BC, derived from the unsteady Bernoulli equation, which expresses the conservation of momentum. These equations describe the dynamics of the total water depth $h(x, y, t) = H(x, y) + \eta(x, y, t)$, where $H(x, y) = H_0 - b(x, y)$ is the depth at rest and

$\eta(x, y, t)$ is the surface deviation from $H(x, y)$ with topography at $z = b(x, y)$, and of the velocity potential $\phi(x, y, z, t)$, which is defined such that the velocity field $\mathbf{u} = (u_x, u_y, u_z)$ may be expressed as $\mathbf{u} = \nabla\phi$. In this study, the nonlinear, potential-flow equations

$$\nabla^2\phi = 0, \text{ in } \Omega, \quad (1a)$$

$$\partial_t h + \nabla(h + b) \cdot \nabla\phi - \partial_z\phi = 0, \quad \text{at } z = b + h, \quad (1b)$$

$$\partial_t\phi + \frac{1}{2}|\nabla\phi|^2 + g(b + h - H_0) = 0, \quad \text{at } z = b + h, \quad (1c)$$

$$\partial_x\phi - \partial_y\phi\partial_y R = \partial_t R \quad \text{at } x = R, \quad (1d)$$

where g is the gravitational constant, are obtained from Luke's variational principle [14] for an inviscid fluid:

$$0 = \delta \int_0^T \int_{\Omega_{x,y}} \int_{b(x,y)}^{b(x,y)+h(x,y,t)} \left[\partial_t\phi + \frac{1}{2}|\nabla\phi|^2 + g(z - H_0) \right] dz dx dy dt. \quad (2)$$

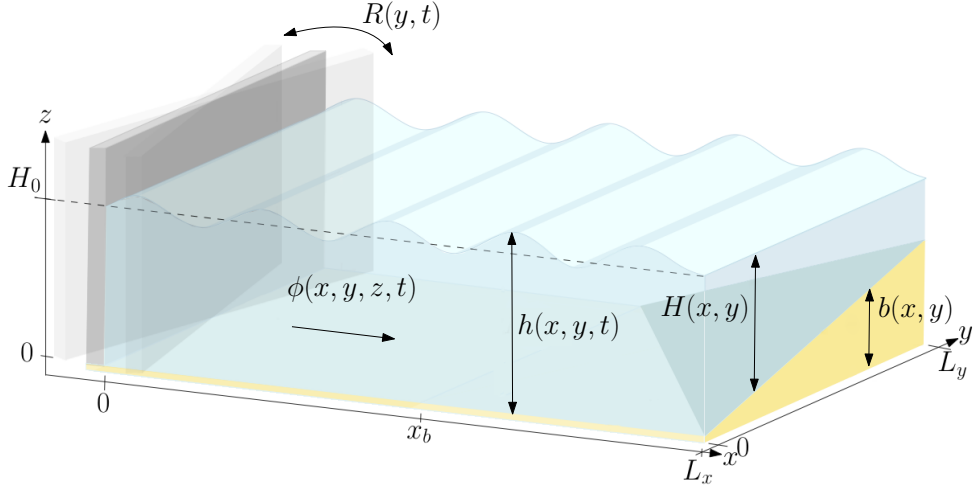


Fig. 1: Schematic of the numerical wave tank. Waves are generated by a vertical piston wavemaker oscillating horizontally at $x = R(y, t)$ around $x = 0$. The depth at rest $H(x, y)$ varies in space due to the nonuniform seabed topography $b(x, y)$, here starting at $x = x_b$.

The horizontal domain $\Omega_{x,y} = \{R(y, t) \leq x \leq L_x; 0 \leq y \leq L_y\}$ is time-dependent due to the wavemaker boundary given by $x = R(y, t)$ (*cf.* Fig. 1). Similarly, the upper boundary of the domain, at $z = b(x, y) + h(x, y, t)$, moves around the rest depth $z = H_0$ with deviation $\eta(x, y, t)$ therefrom. The numerical domain must therefore be discretized with a time-dependent mesh, with moving boundaries at $x = R(y, t)$ and $z = b(x, y) + h(x, y, t)$, noting that the water depth $h(x, y, t)$ is an unknown that itself needs to be solved as part of the solution. A coordinate transform similar to the one introduced by [13] is used to solve the equations on a static domain, such that the transformed upper and moving wavemaker boundaries are fixed so that no vertical mesh movement is required. Extending [13], we therefore introduce an additional coordinate transform in the x -direction to prevent the left-hand boundary from moving in the computational or transformed domain. The resulting computational domain, as represented in Fig. 2, is defined as

$$\hat{\Omega} = \{0 \leq \hat{x} \leq L_x; 0 \leq \hat{y} \leq L_y; 0 \leq \hat{z} \leq H_0\}, \quad (3)$$

where $H_0 = \max_{x \in \Omega_{x,y}} H(x, y)$. It is obtained from the initial domain

$$\Omega = \{R(y, t) \leq x \leq L_x; 0 \leq y \leq L_y; b(x, y) \leq z \leq h(x, y, t) + b(x, y)\}$$

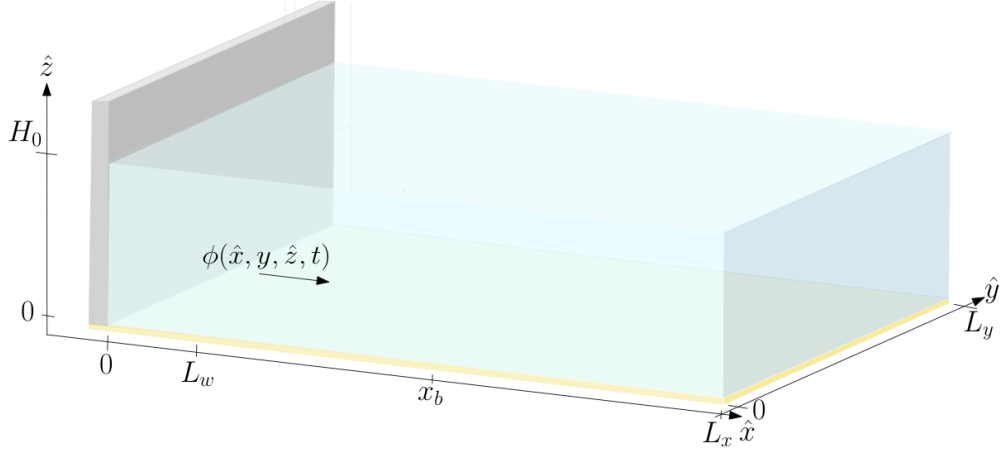


Fig. 2: A depiction of the fixed, computational domain $\hat{\Omega}$ as defined by (3).

through the following transformations:

$$x \rightarrow \hat{x} = \frac{x - \tilde{R}(x, y, t)}{L_w - \tilde{R}(x, y, t)} L_w, \quad (4a)$$

$$y \rightarrow \hat{y} = y, \quad (4b)$$

$$z \rightarrow \hat{z} = (z - b(x, y)) \frac{H_0}{h(x, y, t)}, \quad (4c)$$

$$t \rightarrow \hat{t} = t, \quad (4d)$$

wherein $L_w = O(\lambda)$, with λ being a typical wavelength generated by the wavemaker and

$$\tilde{R}(x, y, t) = R(y, t) \Theta(L_w - x) = \begin{cases} R(y, t), & \text{if } x \leq L_w, \\ 0, & \text{if } x > L_w. \end{cases} \quad (5)$$

In Eq. (5), Θ denotes the Heaviside function such that the coordinate transform is effective in only the area $x \in [R(y, t), L_w]$, with $L_w = O(\lambda)$ as quantified above: in this way, one can couple the water subdomain with the wavemaker without the need to transform in the x -direction for $L_w \leq x \leq L_x$. For example, in our case, the beginning of the seabed topography is set at $x = x_b \gg L_w$ so that $H(\hat{x}, \hat{y}) = H(x, y)$ since the domain is transformed only where the topography is constant, with $H(x, y) = H_0$. The transformation (4) ensures that the new vertical coordinate is contained within $[0, H_0]$ in the whole domain, allowing us to expand solutions on a fixed and prescribed mesh.

Transforming the variational principle (2) by using (4), dropping hats and multiplying by a common factor $H_0 L_w$ leads to (q.v. Appendix A):

$$0 = \delta \int_0^T \left\{ \int_{\hat{\Omega}_{x,y}} \left[\int_0^{H_0} \left[\frac{1}{2} \frac{L_w^2}{W} h \left(\phi_x - \frac{1}{h} (H_0 b_x + z h_x) \phi_z \right)^2 \right. \right. \right. \\ \left. \left. + \frac{1}{2} W h \left(\frac{U}{W} \left[\phi_x - \frac{1}{h} (H_0 b_x + z h_x) \phi_z \right] + \phi_y - \frac{1}{h} (H_0 b_y + z h_y) \phi_z \right)^2 \right. \right. \\ \left. \left. + \frac{1}{2} W \frac{H_0^2}{h} (\phi_z)^2 + W h \left(\phi_t - \frac{z}{h} \left(\frac{X}{W} \tilde{R}_t h_x + h_t \right) \phi_z + \frac{X}{W} \tilde{R}_t \phi_x + g(z \frac{h}{H_0} - H) \right) \right] dz \right] dx dy \right\} dt, \quad (6)$$

in which subscripts denotes partial differentiation and where $\hat{\Omega}_{x,y}$ is the fixed horizontal domain, that is $\hat{\Omega}_{x,y} = \{0 \leq x \leq L_x; 0 \leq y \leq L_y\}$, and where

$$X(x) = x - L_w \quad (7a)$$

$$U(x, y, t) = X \tilde{R}_y(x, y, t), \quad (7b)$$

$$W(x, y, t) = L_w - \tilde{R}(x, y, t). \quad (7c)$$

Using integrations by parts in x, z and t for the last four terms in (6) yields the equivalent of Miles' VP, cf. [23], in transformed coordinates:

$$\begin{aligned} 0 = \delta \int_0^T \left\{ \int_{\hat{\Omega}_{x,y}} \left[\int_0^{H_0} \left[\frac{1}{2} \frac{L_w^2}{W} h(\phi_x - \frac{1}{h}(H_0 \underline{\underline{b}}_x + zh_x)\phi_z)^2 \right. \right. \right. \\ \left. \left. \left. + \frac{1}{2} Wh \left(\frac{U}{W} \left[\phi_x - \frac{1}{h}(H_0 \underline{\underline{b}}_x + zh_x)\phi_z \right] + \phi_y - \frac{1}{h}(H_0 \underline{\underline{b}}_y + zh_y)\phi_z \right)^2 + \frac{1}{2} W \frac{H_0^2}{h} (\phi_z)^2 \right] dz \right. \right. \\ \left. \left. \left. + H_0 \left(gWh \left(\frac{1}{2}h - H \right) - \phi(Wh_t + X \tilde{R}_t h_x) \right) \right]_{z=H_0} dx dy \right. \right. \\ \left. \left. \left. + \int_0^{L_y} \int_0^{H_0} (L_w \tilde{R}_t \phi h)_{x=0} dz dy \right] dt. \right. \right. \end{aligned} \quad (8)$$

Here we used that the term $-(x - L_w) R_t \delta(x - L_w) h \phi$ arising when integrating (6) in x is zero in the weak form since the contribution of $\delta(x - L_w)$ is zero due to the presence of the factor $(x - L_w)$. The transformed nonlinear potential-flow equations may be obtained from the variations of h and ϕ in (6) or (8). Spatial- and temporal-discretization strategies used to solve these equations numerically are described next. Also, it should be noted that the double-underlined gradients of the topography b in the kinetic-energy expression in (8) can be ignored in a so-called *mild-slope approximation*. Simulations with and without this approximation will be performed and analysed.

3. Numerical model

The variational model in the fixed, transformed coordinates (8) forms a basis for overcoming numerical challenges resulting from the nonlinear dynamic boundaries of the computational domain. In this section, we develop cost-effective spatial and temporal discretization schemes.

3.1. Spatial-discretization strategies

To solve the transformed potential-flow equations arising from (8), the domain and the equations must be discretized in space. The finite-element environment Firedrake [17, 18, 19, 20, 21] is used to solve the weak formulations with the finite-element method (see, for example, [24]). Firedrake automates the spatial discretization of partial differential equations internally, based on user-defined settings regarding mesh and polynomial expansions of the variables. While Firedrake simplifies the implementation of our solvers, some challenges arising from the 3D-structure of the waves must first be overcome. Our strategy for doing so is described next.

3.1.1. Updating the vertical structure

In Eq. (1), the functions h and ϕ are updated, through Eq. (1b) and Eq. (1c) respectively, at the free surface only. While h depends on only horizontal spatial coordinates, the velocity potential ϕ depends also on vertical coordinate z , and its subsurface values depend on h and b through the (transformed) Laplace equation Eq. (1a). In order to update ϕ both at the surface and in the interior, we therefore need to distinguish its surface and interior evaluations. For this purpose, we use the Schur-complement method which is based on the Dirichlet-to-Neumann (DtN) operator [25] and aims to decompose the domain into non-overlapping subdomains so that the subsurface subdomains may later be eliminated. Essentially, we discretize the 3D transformed domain $\hat{\Omega}$ with $N_x \times N_y$ quadrilateral elements in the (transformed) horizontal plane, but with only one vertical element, on which the velocity potential is expanded with high-order expansions as

$$\phi(x, y, z, t) = \psi_i(x, y, t) \tilde{\varphi}_i(z), \quad (9)$$

where the Einstein summation convention is used over repeated indices $i \in [1, n_z + 1]$ with index $n_z > 1$. Herein, the vertical component of the velocity potential is expanded as a Lagrange polynomial of order n_z as

$$\tilde{\varphi}_i(z) = \prod_{\substack{k=1 \\ k \neq i}}^{n_z+1} \frac{z - z_k}{z_i - z_k}, \quad (10)$$

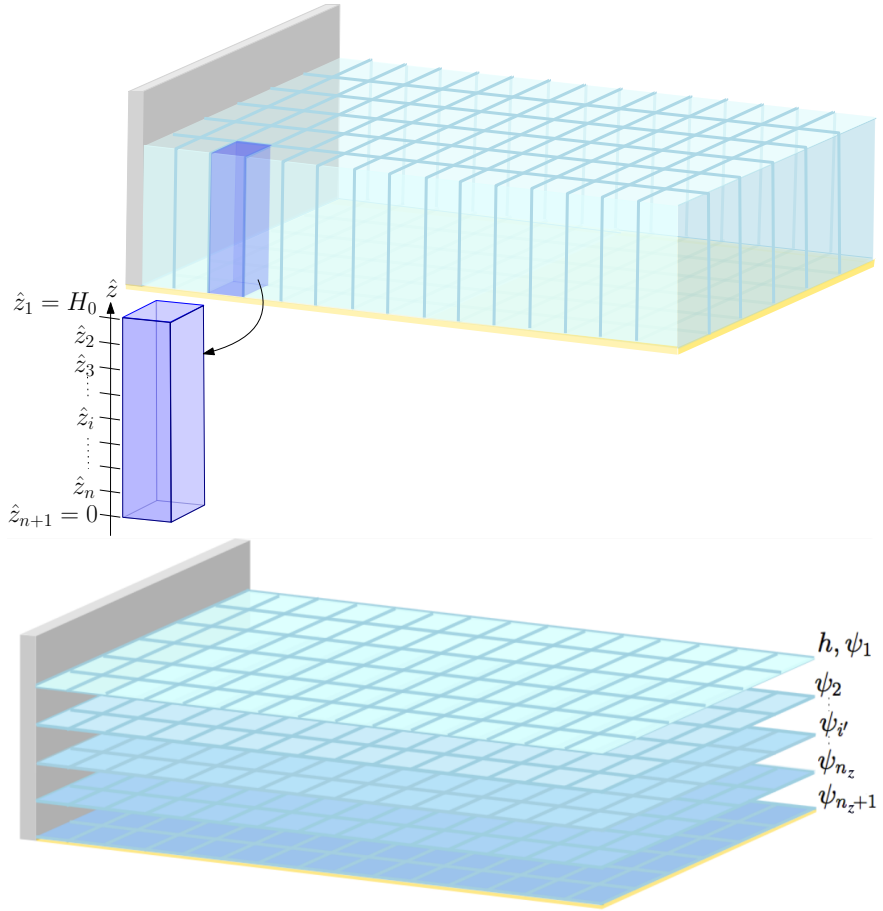


Fig. 3: Top: Discretized 3D fixed domain $\hat{\Omega}_d$. The mesh contains $N_x \times N_y$ elements in the horizontal plane, and one vertical element on which the velocity potential is expanded with high-order expansions in order to deal with the z -dependency of the weak formulations. Bottom: Equivalent discrete domain obtained for solving the transformed Euler equations with the finite-element method. The unknowns are expanded in each horizontal plane with continuous Galerkin expansions.

with discrete vertical nodes z_i defined for all $i \in [1, n_z + 1]$ as

$$z_i = \frac{H_0}{n_z}(n_z + 1 - i). \quad (11)$$

The value of n_z must be set by the user depending on the required vertical resolution. Similarly, the linear distribution in Eq. (11) may be changed to non-uniform points, such as those generated by an exponential distribution. From Eq. (10), the polynomial $\tilde{\varphi}_i$, with $i \in [1, n_z + 1]$, is defined such that

$$\tilde{\varphi}_i(z_k) = \delta_{ik} = \begin{cases} 1 & \text{if } k = i, \\ 0 & \text{if } k \neq i. \end{cases} \quad (12)$$

Our indexing strategy is to set the index $i = 1$ at the surface, and use $i' \in [2, n_z + 1]$ in the interior layers; that is,

$$\begin{cases} z_1 = H_0, \\ 0 \leq z_{i'} < H_0, \end{cases} \quad (13)$$

so that, $\forall i' \in [2, n_z + 1]$, Lagrange-polynomial nodal values are

$$\begin{cases} \tilde{\varphi}_{i'}(H_0) = 0, \\ \tilde{\varphi}_{i'}(z_{i'}) = 1, \end{cases} \quad \text{and} \quad \begin{cases} \tilde{\varphi}_1(H_0) = 1, \\ \tilde{\varphi}_1(z_{i'}) = 0. \end{cases} \quad (14)$$

As a consequence, the surface and interior evaluations of the velocity potential may be distinguished through

$$\phi(x, y, z, t) = \begin{cases} \psi_1(x, y, t) & \text{at the surface } z = z_1 = H_0, \\ \psi_{i'}(x, y, t) & \text{on a horizontal plane } i' \text{ defined by } z = z_{i'} < H_0, \\ \sum_{j=1}^{n_z+1} \psi_j(x, y, t) \tilde{\varphi}_j(z) & \text{for } z \neq z_i, \forall i \in [1, n_z + 1]. \end{cases} \quad (15)$$

For the sake of clarity, primes are removed in the rest of the paper. Figure 3 illustrates the discrete mesh. By distinguishing the surface and interior evaluations one can obtain a variational principle for $n_z + 2$ unknowns comprising the depth h , the velocity potential ψ_1 at the surface and the n_z interior velocity potentials ψ_i , henceforth considered *en bloc* as a column vector $\hat{\psi}$ of dimension $N = n_z$ whose $(i - 1)^{\text{th}}$ element is ψ_i for $i \in [2, n_z + 1]$. Element-by-element spatial partial differentiation of $\hat{\psi}(x, y, t)$ is denoted by $\hat{\psi}_x$ and $\hat{\psi}_y$. Substitution of Eq. (9) rewritten as $\phi = \psi_1 \tilde{\varphi}_1 + \psi_i \tilde{\varphi}_i$ into the variational principle (8) enables separation (and computation) of z -integrals from x - and y -integrals as follows, in which all $(N + 1) \times (N + 1)$ matrices \tilde{A} , say, are partitioned as

$$\tilde{A} = \begin{pmatrix} A_{11} & A_{1N}^T \\ A_{N1} & A_{NN} \end{pmatrix}. \quad (16)$$

Using the aforementioned notation, the variational principle (8) yields

$$\begin{aligned} 0 = \delta \int_0^T \left\{ \int_{\tilde{\Omega}_{x,y}} \left[\frac{h}{2} \left(\tilde{M}_{11} \bar{\nabla}(\psi_1, \psi_1) + 2\psi_{1,x} \tilde{M}_{1N}^T \left(\frac{V}{W} \hat{\psi}_x + U \hat{\psi}_y \right) + 2\psi_{1,y} \tilde{M}_{1N}^T \left(U \hat{\psi}_x + W \hat{\psi}_y \right) \right. \right. \right. \\ \left. \left. \left. + \frac{V}{W} \hat{\psi}_x^T \tilde{M}_{NN} \hat{\psi}_x + 2U \hat{\psi}_x^T \tilde{M}_{NN} \hat{\psi}_y + W \hat{\psi}_y^T \tilde{M}_{NN} \hat{\psi}_y \right) \right. \right. \\ \left. \left. + \frac{1}{2h} \left(\psi_1 \tilde{S}_{11} \psi_1 + 2\psi_1 \tilde{S}_{1N}^T \hat{\psi} + \hat{\psi}^T \tilde{S}_{NN} \hat{\psi} \right) \bar{\nabla}(h, h) \right. \right. \\ \left. \left. + \frac{H_0^2}{2h} \left(\psi_1 \tilde{A}_{11} \psi_1 + 2\psi_1 \tilde{A}_{1N}^T \hat{\psi} + \hat{\psi}^T \tilde{A}_{NN} \hat{\psi} \right) (\bar{\nabla}(b, b) + W) \right. \right. \\ \left. \left. + \frac{H_0}{h} \left(\psi_1 \tilde{C}_{11} \psi_1 + 2\psi_1 \tilde{C}_{1N}^T \hat{\psi} + \hat{\psi}^T \tilde{C}_{NN} \hat{\psi} \right) \bar{\nabla}(b, h) \right. \right. \\ \left. \left. - \left((\bar{\nabla}(h, \psi_1) \tilde{D}_{11} + \bar{\nabla}(h, \hat{\psi})^T \tilde{D}_{N1}) \psi_1 + (\bar{\nabla}(h, \psi_1) \tilde{D}_{1N}^T + \bar{\nabla}(h, \hat{\psi})^T \tilde{D}_{NN}) \hat{\psi} \right) \right. \right. \\ \left. \left. - H_0 \left((\bar{\nabla}(b, \psi_1) \tilde{B}_{11} + \bar{\nabla}(b, \hat{\psi})^T \tilde{B}_{N1}) \psi_1 + (\bar{\nabla}(b, \psi_1) \tilde{B}_{1N}^T + \bar{\nabla}(b, \hat{\psi})^T \tilde{B}_{NN}) \hat{\psi} \right) \right. \right. \\ \left. \left. + H_0 \left(gWh \left(\frac{1}{2}h - H \right) - \psi_1 Wh_t - \underline{\psi_1 X \tilde{R}_t h_x} \right) \right] dx dy + \underbrace{\int_0^{L_y} \left(L_w \tilde{R}_t (\psi_1 \tilde{I}_1 + \hat{\psi}^T \tilde{I}_N) h \right)_{x=0} dy \right\} dt, \right. \right. \end{aligned} \quad (17)$$

in which the matrices \tilde{A} , \tilde{B} , \tilde{C} , \tilde{D} , \tilde{I} , \tilde{S} and \tilde{M} are defined as

$$\begin{aligned} \tilde{I}_i &= \int_0^{H_0} \tilde{\varphi}_i(z) dz, & \tilde{B}_{ij} &= \int_0^{H_0} \tilde{\varphi}_i(z) \frac{d\tilde{\varphi}_j(z)}{dz} dz, & \tilde{A}_{ij} &= \int_0^{H_0} \frac{d\tilde{\varphi}_i(z)}{dz} \frac{d\tilde{\varphi}_j(z)}{dz} dz, \\ \tilde{M}_{ij} &= \int_0^{H_0} \tilde{\varphi}_i(z) \tilde{\varphi}_j(z) dz, & \tilde{D}_{ij} &= \int_0^{H_0} z \tilde{\varphi}_i(z) \frac{d\tilde{\varphi}_j(z)}{dz} dz, & \tilde{C}_{ij} &= \int_0^{H_0} z \frac{d\tilde{\varphi}_i(z)}{dz} \frac{d\tilde{\varphi}_j(z)}{dz} dz, \\ & & & & \tilde{S}_{ij} &= \int_0^{H_0} z^2 \frac{d\tilde{\varphi}_i(z)}{dz} \frac{d\tilde{\varphi}_j(z)}{dz} dz, \end{aligned} \quad (18)$$

and the operator $\bar{\nabla}$ is a bilinear gradient operator defined as

$$\bar{\nabla}(f, g) \equiv \frac{V}{W} f_x g_x + U (f_x g_y + f_y g_x) + W f_y g_y, \quad (19)$$

with

$$V(x, y, t) = L_w^2 + U^2(x, y, t). \quad (20)$$

Note that, in (17), some compression occurs through the symmetry of \tilde{A} , \tilde{C} , \tilde{S} and \tilde{M} , and the notation $\bar{\nabla}(h, \hat{\psi})$ denotes, by the linearity in $\hat{\psi}$ implied by (19) with $f = h$ and $g = \hat{\psi}$, an N -vector whose $(i - 1)^{\text{th}}$ element is $\bar{\nabla}(h, \psi_i)$ for $i \in [2, n_z + 1]$; the term $\bar{\nabla}(b, \hat{\psi})$ follows analogously.

Variations of (17) with respect to each component of $\hat{\psi}$ lead to the n_z equations describing the evolution of the velocity potential in each interior layer of the domain, enabling an update of $\phi(x, y, z, t)$ in the three-dimensional domain. Details of how the transformed water-wave equations are obtained by taking variations of (17) with respect to h , ψ_1 , and each ψ_i for $i \in [2, n_z + 1]$ are deferred to Appendix B. The resulting equations are implemented in the open-source Firedrake environment, in which the finite-element method is used to expand the variables h , ψ_1 and $\hat{\psi}$ in the horizontal plane.

In more abstract form, with the vector $\hat{\psi}$, (17) can be rewritten as follows

$$0 = \delta \int_0^T \left\{ \int_{\hat{\Omega}_{x,y}} -H_0 W \psi_1 \partial_t h \, dx \, dy + \mathcal{H}[h, \psi_1, \hat{\psi}; R] + \underline{\mathcal{R}[h, \psi_1, \hat{\psi}; R]} \right\} dt \quad (21)$$

with the underlined terms in (17) collected in \mathcal{R} , whilst \mathcal{H} still depends on R (and thus explicitly on time t) but only through $U = X\tilde{R}_y$ and $W = L_w - \tilde{R}$. Also, \mathcal{R} is linear in ψ_1 and $\hat{\psi}$. Variations of (21) yield the following equations in abstract format: in them, and in (21) above, terms that appear linearly in the integral expressions have been placed before the semi-colon, as follows

$$\int_{\hat{\Omega}_{x,y}} H_0 \partial_t (W \psi_1) \delta h \, dx \, dy = -(\delta h; h, \psi_1, \hat{\psi}, R)_{\delta \mathcal{H}_h} - (\delta h; h, \psi_1, \hat{\psi}, R)_{\delta \mathcal{R}_h}, \quad (22a)$$

$$\int_{\hat{\Omega}_{x,y}} H_0 \partial_t h \delta (W \psi_1) \, dx \, dy = (\delta \psi_1; h, \psi_1, \hat{\psi}, R)_{\delta \mathcal{H}_{\psi_1}} + (\delta \psi_1; h, \hat{\psi}, R)_{\delta \mathcal{R}_{\psi_1}}, \quad (22b)$$

with

$$(\delta \hat{\psi}; h, \psi_1, \hat{\psi}, R)_{\delta \mathcal{H}_{\hat{\psi}}} = -(\delta \hat{\psi}; h, R)_{\delta \mathcal{R}_{\hat{\psi}}} \implies (\delta \hat{\psi}, \hat{\psi}; h, R)_{\delta \mathcal{H}_{\hat{\psi},2}} = -(\delta \hat{\psi}, \psi_1; h, R)_{\delta \mathcal{H}_{\hat{\psi},1}} - (\delta \hat{\psi}; h, R)_{\delta \mathcal{R}_{\hat{\psi}}}; \quad (22c)$$

herein (22c) being the discretization of the Laplace equation. In (22c), variations with respect to $\hat{\psi}$ of both \mathcal{H} and \mathcal{R} are linear in $\hat{\psi}$ and ψ_1 .

Note that (22a) is bilinear since the kinetic energy term is quadratic in $(\psi_1, \hat{\psi})^T$. Subscripts in the above expressions denote variations with respect to the chosen variable, and the variation with respect to $\hat{\psi}$ has two components, one linear in $\hat{\psi}$ and another linear in ψ_1 , distinguished by extra subscripts 2 and 1 respectively. Full definitions of all terms in (22) are deferred to Appendix B.

3.2. Time discretization

The time integration scheme is developed by first considering an abstract finite-dimensional formulation with a similar structure as in (22) before applying the derived outcomes to the weak formulations given in the previous subsection.

We start with a variational principle for a non-autonomous Hamiltonian system of the form

$$0 = \delta \int_0^T \mathbf{p} \cdot \dot{\mathbf{q}} - H(\mathbf{p}, \mathbf{q}, t) \, dt, \quad (23)$$

with the dot indicating a time derivative. This is appropriate since the variational principle (21) has an additional explicit time dependency through the terms with U, W and thus \tilde{R} . Bokhove and Kalogirou [26] showed that non-autonomous Hamiltonian systems may be expressed as autonomous systems by introducing a new time coordinate τ , by taking t as a variable and by introducing its conjugate, such that $t = t(\tau)$ is an auxiliary variable, with $dt/d\tau = 1$ and $t(0) = 0$. Here we consider a variation thereof. We transform the Hamiltonian $H(\mathbf{q}, \mathbf{p}, t)$ into a so-called ‘‘Kamiltonian’’ system, defined as $K(\mathbf{q}, \mathbf{p}, t, p) = H(\mathbf{q}, \mathbf{p}, t) - q$, for which the new energy K is conserved and the standard autonomous Hamiltonian equations deriving from variational principle

$$0 = \delta \int_0^T \tilde{\mathbf{P}} \cdot \dot{\tilde{\mathbf{Q}}} - K(\tilde{\mathbf{P}}, \tilde{\mathbf{Q}}, t) \, dt, \quad (24)$$

are recovered for the new (vector) pair of conjugate variables $\tilde{\mathbf{P}} = (\mathbf{p}, t)$ and $\tilde{\mathbf{Q}} = (\mathbf{q}, q)$ with the dot now indicating a time derivative with respect to τ .

Rather than looking at the classical Hamiltonian system with generalised coordinates and their conjugates, we instead consider a system augmented with the degrees of freedom associated with the interior of the fluid. The variational principle with the required structure relevant to (21) is now posited to read

$$\begin{aligned} 0 &= \delta \int_0^T \mathbf{p} \cdot \dot{\mathbf{q}} + t \dot{q} - K(\mathbf{P}, \mathbf{p}, \mathbf{q}, t, p) d\tau \\ &\equiv \delta \int_0^T \mathbf{p} \cdot \dot{\mathbf{q}} + t \dot{q} \\ &\quad - \left(\frac{1}{2} \left(\mathbf{p}^T A_{pp}(\mathbf{q}, t) \mathbf{p} + 2 \mathbf{p}^T A_{pP}(\mathbf{q}, t) \mathbf{P} + \mathbf{P}^T A_{PP}(\mathbf{q}, t) \mathbf{P} \right) + V(\mathbf{q}, t) + \mathbf{R}_p(\mathbf{q}, t) \cdot \mathbf{p} + \mathbf{R}_P(\mathbf{q}, t) \cdot \mathbf{P} - q \right) d\tau \end{aligned} \quad (25)$$

with \mathbf{q}, \mathbf{p} vectors with N_s components, associated with the surface degrees of freedom, and \mathbf{P} having $N_s M$ components, with $M = n_z$ associated with the interior degrees of freedom in the vertical. The submatrices A_{pp}, A_{pP}, A_{PP} used above are therefore parts of a $N_s(M+1) \times N_s(M+1)$ symmetric matrix A . In addition, we have introduced vectors \mathbf{R}_p and \mathbf{R}_P . Here \mathbf{q}, \mathbf{p} represent the surface degrees of freedom after a finite-element expansion in the horizontal of h, ψ_1 and \mathbf{P} the interior degrees of freedom after a finite-element expansion in the horizontal of ψ_i . The system ensuing from (25) reads

$$\delta \mathbf{p} : \dot{\mathbf{q}} = + \frac{\partial K}{\partial \mathbf{p}} = A_{pp} \mathbf{p} + A_{pP} \mathbf{P} + \mathbf{R}_p \quad (26a)$$

$$\delta \mathbf{q} : \dot{\mathbf{p}} = - \frac{\partial K}{\partial \mathbf{q}} = - \frac{1}{2} (\mathbf{p}^T, \mathbf{P}^T) \frac{\partial A}{\partial \mathbf{q}} \begin{pmatrix} \mathbf{p} \\ \mathbf{P} \end{pmatrix} - \frac{\partial V}{\partial \mathbf{q}} - \frac{\partial \mathbf{R}_p}{\partial \mathbf{q}} \cdot \mathbf{p} - \frac{\partial \mathbf{R}_P}{\partial \mathbf{q}} \cdot \mathbf{P} \quad (26b)$$

$$\delta \mathbf{P} : \frac{\partial K}{\partial \mathbf{P}} = 0 \implies A_{PP} \mathbf{P} = -A_{pP} \mathbf{p} - \mathbf{R}_P \implies \mathbf{P} = -A_{pp}^{-1}(\mathbf{q}, t) (A_{pp}(\mathbf{q}, t) \mathbf{p} + \mathbf{R}_p(\mathbf{q}, t)) \quad (26c)$$

$$\delta t : \dot{q} = \frac{\partial K}{\partial t} \quad (26d)$$

$$\delta q : \dot{t} = - \frac{\partial K}{\partial q} = 1, \quad (26e)$$

with the last equation implying that $t = \tau$ when $t(\tau = 0) = 0$. Note that the condensed quadratic form in (26b) uses the full (suffix-free) matrix A . Notably, (26) has the same structure as our finite-element and polynomial spatial discretization, with (26c) being linear in \mathbf{P} and \mathbf{p} , as it represents the discretization of the potential-flow Laplace equation. In addition, we assume that A_{pp} is invertible, which implies that we can eliminate the \mathbf{P} degrees of freedom. However, such elimination is computationally inefficient, so we develop time discretizations for the entire system, including \mathbf{P} , but develop the numerical scheme whilst implicitly eliminating \mathbf{P} in order to find the right time levels for \mathbf{P} . Once this elimination is done (implicitly), the new conjugate variables satisfy the autonomous Hamiltonian system (24) and are again $\tilde{\mathbf{P}} = (\mathbf{p}, t)$ and $\tilde{\mathbf{Q}} = (\mathbf{q}, q)$.

3.2.1. Discontinuous Galerkin time integrators

Emphasising a graphical representation, Bokhove and Kalogirou [26], and also Gagarina *et al.* [16], derived symplectic-Euler and Störmer-Verlet time discretizations of expressions similar to (24) and (25), starting with discontinuous Galerkin finite-element expansions in time on N time intervals $[t^n, t^{n+1}]$ with $n \in [0, N-1]$. Hence, polynomial approximations $\tilde{\mathbf{P}}^\tau$ and $\tilde{\mathbf{Q}}^\tau$ of $\tilde{\mathbf{P}}$ and $\tilde{\mathbf{Q}}$, respectively, are taken to be continuous within the open interval or time slab (t_n, t_{n+1}) but *a priori* taken as discontinuous across each interface/node at $t = t_n$. Papers [26, 16] showed that the symplectic-Euler scheme is a leading-order genuinely discontinuous Galerkin time stepping scheme with constant values in a time-interval, while the Störmer-Verlet scheme is a mixed continuous and discontinuous Galerkin expansion.

Novel to the present approach is that we start directly by discretizing the Kamiltonian variational principle (24),

which in symplectic-Euler discretized form reads

$$\mathbf{Q}^{n+1} = \mathbf{Q}^n + \Delta t \frac{\partial K(\mathbf{Q}^{n+1}, \tilde{\mathbf{P}}^n)}{\partial \tilde{\mathbf{P}}^n} \quad (27a)$$

$$\tilde{\mathbf{P}}^{n+1} = \tilde{\mathbf{P}}^n - \Delta t \frac{\partial K(\mathbf{Q}^{n+1}, \tilde{\mathbf{P}}^n)}{\partial \mathbf{Q}^{n+1}}, \quad (27b)$$

which generally has an implicit first step and an effectively explicit second step. Furthermore, a Störmer-Verlet discretization resulting from (24) reads

$$\tilde{\mathbf{P}}^{n+1/2} = \tilde{\mathbf{P}}^n - \frac{1}{2} \Delta t \frac{\partial K(\mathbf{Q}^n, \tilde{\mathbf{P}}^{n+1/2})}{\partial \mathbf{Q}^n} \quad (28a)$$

$$\mathbf{Q}^{n+1} = \mathbf{Q}^n + \frac{1}{2} \Delta t \left(\frac{\partial K(\mathbf{Q}^n, \tilde{\mathbf{P}}^{n+1/2})}{\partial \tilde{\mathbf{P}}^{n+1/2}} + \frac{\partial K(\mathbf{Q}^{n+1}, \tilde{\mathbf{P}}^{n+1/2})}{\partial \tilde{\mathbf{P}}^{n+1/2}} \right) \quad (28b)$$

$$\tilde{\mathbf{P}}^{n+1} = \tilde{\mathbf{P}}^{n+1/2} - \frac{1}{2} \Delta t \frac{\partial K(\mathbf{Q}^{n+1}, \tilde{\mathbf{P}}^{n+1/2})}{\partial \mathbf{Q}^{n+1}}, \quad (28c)$$

which has generally implicit first two steps and an effectively explicit last step. These two schemes are standard time-stepping found in various textbooks, e.g. [27, 28].

From (27) with $\tilde{\mathbf{P}} = (\mathbf{p}, t)$ and $\mathbf{Q} = (\mathbf{q}, q)$ as well as $\mathbf{P} = \mathbf{P}(\mathbf{q}, \mathbf{p}, t)$, it follows that a symplectic-Euler discretization, cf. [27, 26], of (26), then becomes

$$\mathbf{q}^{n+1} = \mathbf{q}^n + \Delta t \left(A_{pp}(\mathbf{q}^{n+1}, t^n) \mathbf{p}^n + A_{pP}(\mathbf{q}^{n+1}, t^n) \mathbf{P}^* + \mathbf{R}_p(\mathbf{q}^{n+1}, t^n) \right) \quad (29a)$$

$$A_{PP}(\mathbf{q}^{n+1}, t^n) \mathbf{P}^* = -A_{Pp}(\mathbf{q}^{n+1}, t^n) \mathbf{p}^n - \mathbf{R}_P(\mathbf{q}^{n+1}, t^n) \quad (29b)$$

$$\begin{aligned} \mathbf{p}^{n+1} &= \mathbf{p}^n - \Delta t \left(\frac{1}{2} ([\mathbf{p}^n]^T, [\mathbf{P}^*]^T) \frac{\partial A(\mathbf{q}^{n+1}, t^n)}{\partial \mathbf{q}^{n+1}} \begin{pmatrix} \mathbf{p}^n \\ \mathbf{P}^* \end{pmatrix} \right. \\ &\quad \left. + \frac{\partial V(\mathbf{q}^{n+1}, t^n)}{\partial \mathbf{q}^{n+1}} + \frac{\partial \mathbf{R}_p(\mathbf{q}^{n+1}, t^n)}{\partial \mathbf{q}^{n+1}} \cdot \mathbf{p}^n + \frac{\partial \mathbf{R}_P(\mathbf{q}^{n+1}, t^n)}{\partial \mathbf{q}^{n+1}} \cdot \mathbf{P}^* \right), \end{aligned} \quad (29c)$$

in which the auxiliary variable \mathbf{P}^* can be determined by iterative solution of the coupled (29a) and (29b) without having to explicitly invert $A_{PP}(\mathbf{q}^{n+1}, t^n)$. From (28) with $\tilde{\mathbf{P}} = (\mathbf{p}, t)$ and $\mathbf{Q} = (\mathbf{q}, q)$ as well as $\mathbf{P} = \mathbf{P}(\mathbf{q}, \mathbf{p}, t)$, a Störmer-Verlet discretization [27, 26] of (26) then becomes

$$\begin{aligned} \mathbf{p}^{n+1/2} &= \mathbf{p}^n - \frac{1}{2} \Delta t \left(\frac{1}{2} ([\mathbf{p}^{n+1/2}]^T, [\mathbf{P}^*]^T) \frac{\partial A(\mathbf{q}^n, t^{n+1/2})}{\partial \mathbf{q}^n} \begin{pmatrix} \mathbf{p}^{n+1/2} \\ \mathbf{P}^* \end{pmatrix} \right. \\ &\quad \left. + \frac{\partial V(\mathbf{q}^n, t^{n+1/2})}{\partial \mathbf{q}^n} + \frac{\partial \mathbf{R}_p(\mathbf{q}^n, t^{n+1/2})}{\partial \mathbf{q}^n} \cdot \mathbf{p}^n + \frac{\partial \mathbf{R}_P(\mathbf{q}^n, t^{n+1/2})}{\partial \mathbf{q}^n} \cdot \mathbf{P}^* \right) \end{aligned} \quad (30a)$$

$$A_{PP}(\mathbf{q}^n, t^{n+1/2}) \mathbf{P}^* = -A_{Pp}(\mathbf{q}^n, t^{n+1/2}) \mathbf{p}^{n+1/2} - \mathbf{R}_P(\mathbf{q}^n, t^{n+1/2}) \quad (30b)$$

$$\begin{aligned} \mathbf{q}^{n+1} &= \mathbf{q}^n + \frac{1}{2} \Delta t \left(\left(A_{pp}(\mathbf{q}^n, t^{n+1/2}) \mathbf{p}^{n+1/2} + A_{pP}(\mathbf{q}^n, t^{n+1/2}) \mathbf{P}^* + \mathbf{R}_p(\mathbf{q}^n, t^{n+1/2}) \right) \right. \\ &\quad \left. + \left(A_{pp}(\mathbf{q}^{n+1}, t^{n+1/2}) \mathbf{p}^{n+1/2} + A_{pP}(\mathbf{q}^{n+1}, t^{n+1/2}) \mathbf{P}^* + \mathbf{R}_p(\mathbf{q}^{n+1}, t^{n+1/2}) \right) \right) \end{aligned} \quad (30c)$$

$$A_{PP}(\mathbf{q}^{n+1}, t^{n+1/2}) \mathbf{P}^* = -A_{Pp}(\mathbf{q}^{n+1}, t^{n+1/2}) \mathbf{p}^{n+1/2} - \mathbf{R}_P(\mathbf{q}^{n+1}, t^{n+1/2}) \quad (30d)$$

$$\begin{aligned} \mathbf{p}^{n+1} &= \mathbf{p}^{n+1/2} - \frac{1}{2} \Delta t \left(\frac{1}{2} ([\mathbf{p}^{n+1/2}]^T, [\mathbf{P}^*]^T) \frac{\partial A(\mathbf{q}^{n+1}, t^{n+1/2})}{\partial \mathbf{q}^{n+1}} \begin{pmatrix} \mathbf{p}^{n+1/2} \\ \mathbf{P}^* \end{pmatrix} \right. \\ &\quad \left. + \frac{\partial V(\mathbf{q}^{n+1}, t^{n+1/2})}{\partial \mathbf{q}^{n+1}} + \frac{\partial \mathbf{R}_p(\mathbf{q}^{n+1}, t^{n+1/2})}{\partial \mathbf{q}^{n+1}} \cdot \mathbf{p}^{n+1/2} + \frac{\partial \mathbf{R}_P(\mathbf{q}^{n+1}, t^{n+1/2})}{\partial \mathbf{q}^{n+1}} \cdot \mathbf{P}^* \right), \end{aligned} \quad (30e)$$

in which $\mathbf{p}^{n+1/2}$ and the auxiliary variable \mathbf{P}^* is determined by iterative solution of the coupled (30a) and (30b); with \mathbf{q}^{n+1} and \mathbf{P}^* in (30c) and (30d) solved jointly in iterative fashion as well, while \mathbf{p}^{n+1} in (30e) is an explicit step.

Using (29), the symplectic-Euler discretization of (22) becomes

$$\left\{ \begin{array}{l} \int_{\hat{\Omega}_{x,y}} \frac{H_0}{\Delta t} (h^{n+1} - h^n) \delta(W\psi_1) dx dy = (\delta\psi_1; h^{n+1}, \psi_1^n, \hat{\psi}^*, R^n)_{\delta\mathcal{H}_{\psi_1}} + (\delta\psi_1; h^{n+1}, \hat{\psi}^*, R^n)_{\delta\mathcal{R}_{\psi_1}} \\ (\delta\hat{\psi}, \hat{\psi}^*; h^{n+1}, R^n)_{\delta\mathcal{H}_{\hat{\psi}_2}} = -(\delta\hat{\psi}, \psi_1^n; h^{n+1}, R^n)_{\delta\mathcal{H}_{\hat{\psi}_1}} - (\delta\hat{\psi}; h^{n+1}, R^n)_{\delta\mathcal{R}_{\hat{\psi}}} \end{array} \right. \quad (31a)$$

$$\int_{\hat{\Omega}_{x,y}} \frac{H_0}{\Delta t} (W^{n+1}\psi_1^{n+1} - W^n\psi_1^n) \delta h dx dy = -(\delta h; h^{n+1}, \psi_1^n, \hat{\psi}^*, R^n)_{\delta\mathcal{H}_h} - (\delta h; h^{n+1}, \psi_1^n, \hat{\psi}^*, R^n)_{\delta\mathcal{R}_h}. \quad (31b)$$

in which $\hat{\psi}^*$ is a vector of updated sub-surface velocity potentials. Similarly, using (30), the Störmer-Verlet discretization of (22) then becomes

$$\left\{ \begin{array}{l} \int_{\hat{\Omega}_{x,y}} \frac{2H_0}{\Delta t} (W^{n+1/2}\psi_1^{n+1/2} - W^n\psi_1^n) \delta h dx dy = -(\delta h; h^n, \psi_1^{n+1/2}, \hat{\psi}^*, R^{n+1/2})_{\delta\mathcal{H}_h} - (\delta h; h^n, \psi_1^{n+1/2}, \hat{\psi}^*, R^{n+1/2})_{\delta\mathcal{R}_h} \\ (\delta\hat{\psi}, \hat{\psi}^*; h^n, R^{n+1/2})_{\delta\mathcal{H}_{\hat{\psi}_2}} = -(\delta\hat{\psi}, \psi_1^{n+1/2}; h^n, R^{n+1/2})_{\delta\mathcal{H}_{\hat{\psi}_1}} - (\delta\hat{\psi}; h^n, R^{n+1/2})_{\delta\mathcal{R}_{\hat{\psi}}} \end{array} \right. \quad (32a)$$

$$\left\{ \begin{array}{l} \int_{\hat{\Omega}_{x,y}} \frac{2H_0}{\Delta t} (h^{n+1} - h^n) \delta(W\psi_1) dx dy = ((\delta\psi_1; h^n, \psi_1^{n+1/2}, \hat{\psi}^*, R^{n+1/2})_{\delta\mathcal{H}_{\psi_1}} + (\delta\psi_1; h^n, \hat{\psi}^*, R^{n+1/2})_{\delta\mathcal{R}_{\psi_1}} + \\ (\delta\psi_1; h^{n+1}, \psi_1^{n+1/2}, \hat{\psi}^*, R^{n+1/2})_{\delta\mathcal{H}_{\psi_1}} + (\delta\psi_1; h^{n+1}, \hat{\psi}^*, R^{n+1/2})_{\delta\mathcal{R}_{\psi_1}}) \\ (\delta\hat{\psi}, \hat{\psi}^*; h^{n+1}, R^{n+1/2})_{\delta\mathcal{H}_{\hat{\psi}_2}} = -(\delta\hat{\psi}, \psi_1^{n+1/2}; h^{n+1}, R^{n+1/2})_{\delta\mathcal{H}_{\hat{\psi}_1}} - (\delta\hat{\psi}; h^{n+1}, R^{n+1/2})_{\delta\mathcal{R}_{\hat{\psi}}} \end{array} \right. \quad (32b)$$

$$\int_{\hat{\Omega}_{x,y}} \frac{2H_0}{\Delta t} (W^{n+1}\psi_1^{n+1} - W^{n+1/2}\psi_1^{n+1/2}) \delta h dx dy = -(\delta h; h^{n+1}, \psi_1^{n+1/2}, \hat{\psi}^*, R^{n+1/2})_{\delta\mathcal{H}_h} - (\delta h; h^{n+1}, \psi_1^{n+1/2}, \hat{\psi}^*, R^{n+1/2})_{\delta\mathcal{R}_h} \quad (32c)$$

in which $\hat{\psi}^\ddagger$ is a vector of two-step-updated sub-surface velocity potentials.

For both the symplectic-Euler and Störmer-Verlet schemes the time-step restriction, based on analysis of a harmonic oscillator with frequency ω_{\max} (cf. [28]), is [29]

$$\Delta t = CFL(2/\omega_{\max}), \quad (33)$$

with Courant number $CFL < 1$, whereafter we use the dispersion relation for linear water waves, $\omega_{\max} \approx \sqrt{gk \tanh(kH_0)}$, together with wavenumber $k = 2\pi/\Delta x$ in order to estimate the corresponding minimum mesh resolution Δx .

4. Verification and validation of the numerical model

Different aspects of the above-derived “numerical model” are now verified and validated via a quartet of test cases. In the first test case (TC1) it is verified against exact standing-wave solutions of 2D, linear, potential-flow equations in the absence of a wavemaker, and above flat-bottom topography. Spatial and temporal convergence analyses in 3D are then undertaken in the presence of an oscillating wavemaker and non-uniform seabed topography (TC2 and TC3). Finally, the model is validated against wave-tank measurements obtained from an open case concerning wave groups propagating over a flat-bottom topography (TC4).

Noting that no test case contains steep gradients in the seabed topography, we apply a *mild-slope approximation* (MSA) in the computational model to (potentially) improve the efficiency of the simulations; MSA is tantamount to neglecting all terms containing gradients of b in the weak formulations (i.e., the wavy-underlined terms in Appendix C and Appendix D) as well as the energy expression (i.e., \mathcal{H} in (21)). The MSA does not affect TC1 and TC4, in both of which $b(x, y) \equiv 0$. For completeness, additional test cases TC2b and TC3b are considered in which gradients of b are retained in, TC2 and TC3, respectively, thereby enabling comparisons between results that either include or exclude the MSA.

4.1. TC1: Verification against standing-wave solution

To directly verify the accuracy, effectiveness and reliability of the computational model, the code is first tested against exact standing-wave solution of 2D *linear* potential-flow equations for the case with a resting wavemaker and flat bottom:

$$\nabla^2 \phi = 0 \quad \text{on } \Omega, \quad (34a)$$

$$\partial_t \eta = \partial_z \phi \quad \partial_t \phi = -g\eta \quad \text{at } z = H_0. \quad (34b)$$

The exact standing-wave solutions of (34) for η and ϕ in a rectangular domain $(x, z) \in L_x \times H_0$ are given by

$$\eta(x, t) = \cos(kx)[A \cos(\omega t) + B \sin(\omega t)], \quad (35a)$$

$$\phi(x, z, t) = \cos(kx)(e^{kz} + e^{-kz})[-A \sin(\omega t) + B \cos(\omega t)]/\omega, \quad (35b)$$

where $k = 2\pi m/L_x$ is the wave number with m a positive integer, and the dispersion relationship is

$$\omega = \sqrt{gk \tanh(kH_0)}. \quad (35c)$$

Both the symplectic-Euler and Störmer-Verlet time-stepping schemes are implemented in this test case, and the unknowns are initialized with (35a) and (35b). The numerical computation is performed with $L_x = 2\pi$, $m = 2$, $A = B = 0.01$ (thus determining the initial conditions) and, given $H_0 = 1.137$, (35c) determines ω . The number of elements in the x -direction and the layers in the vertical direction are set as $N_x = 126$ and $N_z = 7$, respectively. The time step is set as $\Delta t = \min\{\Delta x, \Delta z\}/\pi$. The simulation stops at $t = 3T_p$, with period $T_p = 2\pi/\omega$. For both schemes, the comparison between the numerical solutions and exact standing-wave solutions for $h(x = 0, t)$, $\phi(x = 0, z = 0, t)$ and $\phi(x = 0, z = H_0, t)$ over time are shown in the second and third row of Fig. 4, plotted as dashed and solid lines respectively. Numerical results agree well with exact solutions for both schemes.

We also monitor the energy evolution of the system over time, which is shown in the top row of Fig. 4 for the two schemes in blue solid lines, to verify the consistency of the temporal schemes. It can be seen that for both schemes the energy shows no drift and has bounded oscillations, while the amplitude for the case using Störmer-Verlet scheme is much smaller than that obtained when using the symplectic-Euler scheme. In addition, the energy evolution is also recorded when case TC1 is recomputed with a halved time resolution, for which the corresponding results are shown as cyan lines in Fig. 4. It can be seen that the amplitude of these oscillations decreases for smaller time steps. For the symplectic-Euler scheme, the variations $\Delta E_{SE}(\Delta t/2)$ are less than half of those for the case with original time step Δt , as indicated by the comparison between $2E_{SE}(\Delta t/2)$ and $E_{SE}(\Delta t)$. However, for the Störmer-Verlet scheme, the amplitudes of the energy variations $\Delta E_{SV}(\Delta t)$ are more than four times larger than those obtained when using the halved time step. It can thus be seen from these linear and quadratic decreases in energy variations that the symplectic-Euler and Störmer-Verlet schemes respectively have first-order and second-order temporal accuracy.

4.2. Convergence analysis

4.2.1. TC2: Spatial convergence

Interpolation with first-order continuous Galerkin polynomials yields second-order accuracy [30]. To verify this spatial accuracy, we solve the nonlinear potential-flow equations with both symplectic-Euler and Störmer-Verlet schemes in a 3D domain with dimensions given in Table 1: time step² $\Delta t = 0.002$ s, nine layers in the vertical, and various horizontal spatial resolutions. The wavemaker motion varies in y and is specified as

$$R(y, t) = \gamma(2y - L_y) \cos(\omega t)/L_y. \quad (36)$$

Simulations are performed over time-period $t \in [0, 7]$ s, throughout which the wavemaker is in motion. We first implement TC2 using the *mild-slope approximation*; the results of TC2b, which uses the same parameters as TC2 in the full formulations, are considered separately in the next section.

First, the spatial resolution is set to $\Delta y = \Delta x = 0.025$ m and the corresponding computed water depth $h_{ex}(x, y, t)$ is used as a reference value. The error \mathcal{E} between h_{ex} and the depths $h_{0.05}(x, y, t)$ and $h_{0.1}(x, y, t)$, computed with resolutions $\Delta y = \Delta x = 0.05$ m and $\Delta y = \Delta x = 0.1$ m respectively, is then computed as the L^2 - and L^∞ -norms of their difference, that is

$$\mathcal{E}_{L^2}(h^n) \equiv \|h^n - h_{ex}^n\|_2 = \sqrt{\sum_i (h_i^n - h_{ex,i}^n)^2}, \quad \text{and} \quad \mathcal{E}_{L^\infty}(h^n) \equiv \|h^n - h_{ex}^n\|_\infty = \max_i |h_i^n - h_{ex,i}^n|, \quad (37)$$

where i designates the common nodes between the three meshes, that is, the nodes on the largest mesh. For n^{th} -order accuracy in space, mesh-size halving should yield

$$\mathcal{E}(h_{2\Delta x}) = 2^n \mathcal{E}(h_{\Delta x}) \Rightarrow n = \frac{\ln(\mathcal{E}(h_{2\Delta x})) - \ln(\mathcal{E}(h_{\Delta x}))}{\ln(2)} = \frac{\ln(\mathcal{E}(h_{2\Delta x})) - \ln(\mathcal{E}(h_{\Delta x}))}{\ln(2\Delta x) - \ln(\Delta x)}, \quad (38)$$

²Results obtained using time steps $\Delta t = 0.001$ s and $\Delta t = 0.002$ s were similar; the latter coarser results were used in TC2 and TC2b.

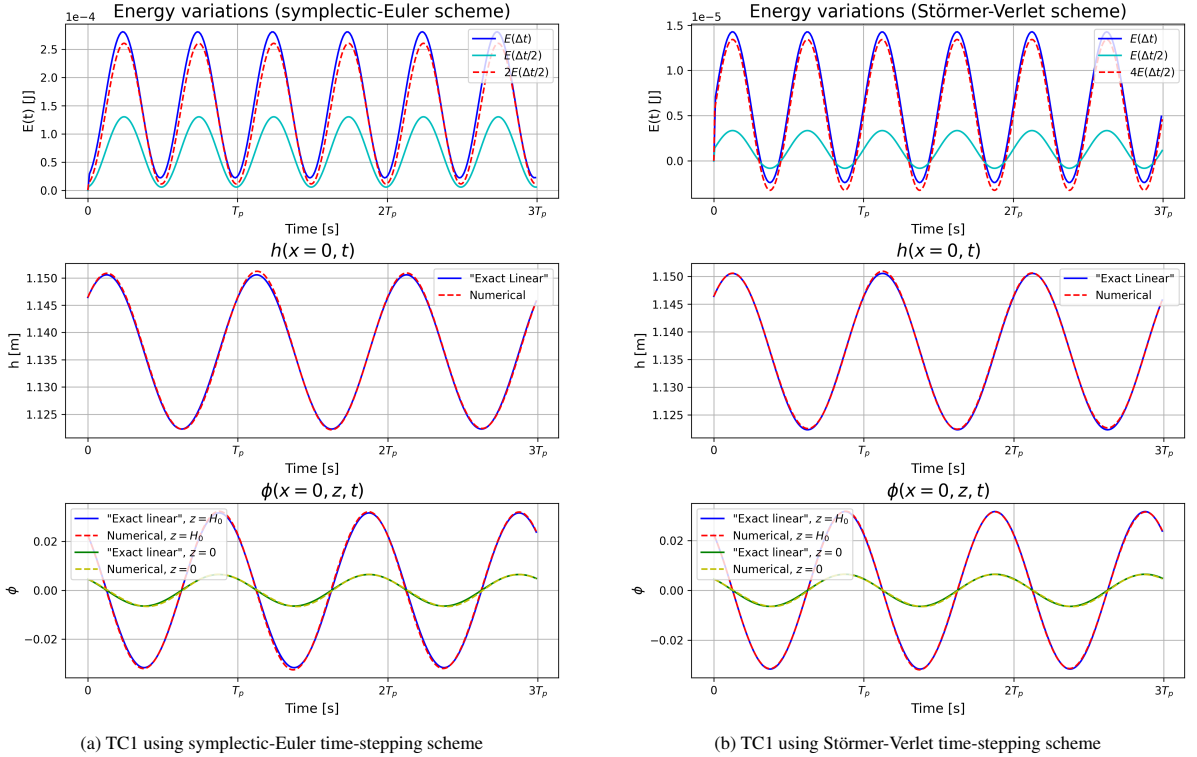


Fig. 4: TC1: Energy variations (top row) and comparison between the numerical solutions and exact standing-wave solutions of linear potential-flow equations (middle and bottom rows) using (a) symplectic-Euler time-stepping scheme and (b) Störmer-Verlet time-stepping scheme.

which is the slope of the chord on the curve $\{x = \ln(\alpha\Delta x), y = \ln(\mathcal{E}(h_{\alpha\Delta x}))\}$ parameterised by α ; here we define the chord by values $\alpha \in \{1, 2\}$. Accordingly, we compute the spatial-convergence indices

$$\beta_{L^2}^n = \frac{\ln(\mathcal{E}_{L^2}(h_{0.1}^n)) - \ln(\mathcal{E}_{L^2}(h_{0.05}^n))}{\ln(0.1) - \ln(0.05)} \quad \text{and} \quad \beta_{L^\infty}^n = \frac{\ln(\mathcal{E}_{L^\infty}(h_{0.1}^n)) - \ln(\mathcal{E}_{L^\infty}(h_{0.05}^n))}{\ln(0.1) - \ln(0.05)} \quad (39)$$

for $t \in [0, 7]$ s, which converge towards the expected order of convergence $n = 2$. The left panels of Fig. 5 show the temporal evolution of β_{L^∞} (top) and β_{L^2} (bottom) and their convergence towards $\beta \approx 2$. This second-order spatial convergence is confirmed in the ln-ln plots in the right panels of Fig. 5 for L^∞ (top) and L^2 (bottom) errors against spatial resolution, together with slopes $\bar{\beta}_{L^\infty}$ and $\bar{\beta}_{L^2}$, computed by averaging β_{L^∞} and β_{L^2} between $t = 4.0$ s and $t = 7.0$ s. Coefficients β_{L^2} and β_{L^∞} converge to $n \approx 2.0$, confirming this convergence rate, whence the spatial accuracy of the solvers is verified.

4.2.2. TC2b: Spatial convergence without the mild-slope approximation

Case TC2 discussed immediately above is now adapted to remove the mild-slope approximation (MSA), resulting in TC2b that employs full energy expressions and full weak formulations (FWF). That is, all terms born of gradients b_x and b_y of seabed topography are adopted in the computational model. Some resulting differences between TC2 and TC2b are shown in Fig. 6 through comparisons (computed on the finest spatial mesh) between energy variations and water depths evaluated at the two right-hand vertices of the wave tank, where not only are absolute values plotted in Fig. 6 (a), but also their corresponding relative errors are calculated as shown in Fig. 6 (b). Fig. 6 reveals that the MSA has only a minor effect on the energy variations, whose maximum relative error has order $O(10^{-6})$, whereas, for the water depth, especially for those located in the zone where $\nabla b \neq \mathbf{0}$, the amplitudes are larger when b_x and b_y are included, though the corresponding differences are small in a relative sense, being order $O(0.1\%)$. In addition, Fig. 7 shows that the temporal evolution of both the spatial-convergence indices β and the order of convergence for TC2b are nearly the same as those for TC2. Therefore, it seems reasonable to adopt the MSA in the computational model when the topography considered is nowhere steep. To further confirm this, we accordingly first retain the MSA in test-case TC3 but then remove it in TC3b, which computationally considers the same seabed slope $s_b = 0.2$ as in TC2b.

Domain				Beach	
L_x [m]	L_y [m]	H_0 [m]	$H(x = L_x)$ [m]	x_b [m]	s_b [-]
4.0	0.8	1.0	0.5	1.5	0.2
Wavemaker					
λ [m]	k [rad/m]	ω [rad/s]	T_w [s]	γ [m]	L_w [m]
2.0	3.14	5.54	1.13	0.02	0.8

Table 1: Parameters used in test cases TC2 and TC2b. Dimensions are given in square brackets. The wavenumber k is determined using the linear water-wave dispersion relationship, whence $\lambda = 2\pi/k$. The wavemaker period is defined as $T_w = 2\pi/\omega$. Seabed topography is set as $b(x) = s_b(x - x_b)\Theta(x - x_b)$.

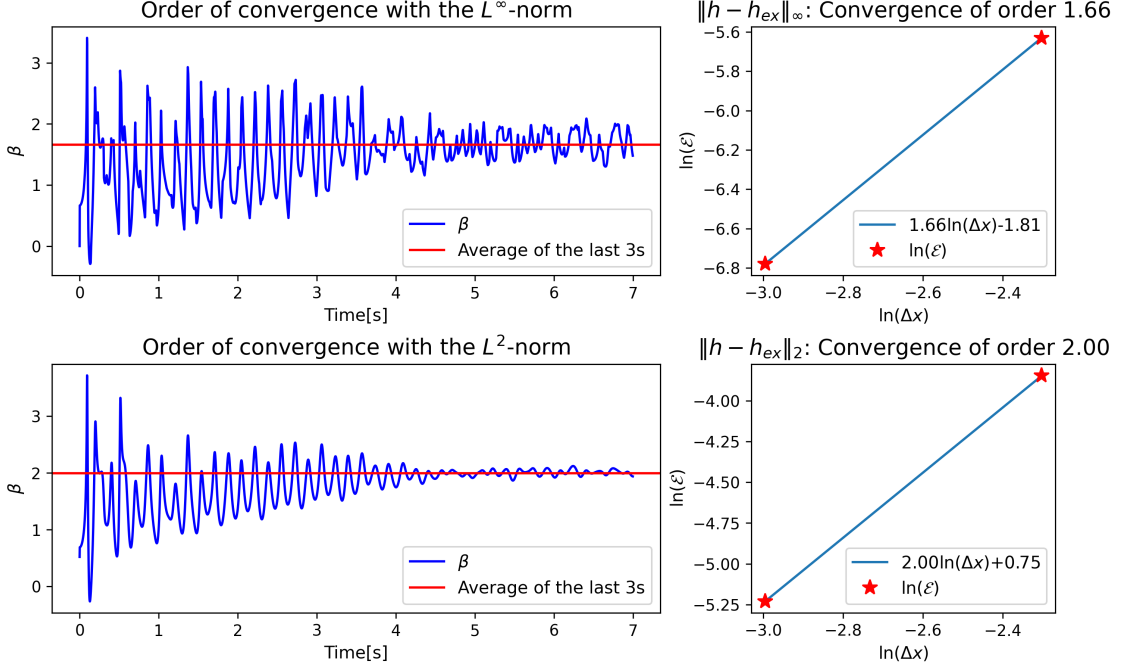


Fig. 5: TC2: Temporal evolution of the spatial-convergence indices β as characterized by L^∞ -norm (top row) and L^2 -norm (bottom row) based on results obtained from the Störmer-Verlet scheme. Corresponding results based on the symplectic-Euler scheme are qualitatively and quantitatively similar since both integrators generate similar results for each mesh resolution.

4.2.3. TC3: Energy conservation and temporal convergence

The symplectic temporal schemes derived in section 3.2.1 (cf., Appendix C and Appendix D), are, by construction, intended to yield stability and bounded energy oscillations and to preclude numerical, dissipative drifts of energy. These energy fluctuations are now checked via computations using two time resolutions, $\Delta t_1 = 0.001$ s and $\Delta t_2 = 0.002$ s, for both the symplectic-Euler and Störmer-Verlet schemes, the corresponding cases for the two tests and schemes being hereafter denoted as SE1 and SE2, or SV1 and SV2. Simulations are conducted in the time-period $t \in [0, 17]$ s, and the wavemaker stops at $t = 5T_w = 5.670$ s, where $T_w = 2\pi/\omega$ is the wavemaker period. All parameters used in TC3 are summarized in Table 2. As per the test cases TC2 and TC2b considered above, here TC3 is computed using the MSA; its recomputed non-MSA counterpart TC3b is considered separately in the next section.

Fig. 8 shows the energy evolutions obtained using (a) symplectic-Euler and (b) Störmer-Verlet schemes for two time resolutions. At $t = 0.0$ s the wavemaker is off and the water is at rest. Hence, there is no kinetic energy in the system; for the purposes of analysing only evolutionary changes, the potential energy has been offset to yield a zero datum. When the wavemaker motion starts, energy is given to the system and energy thus increases on average until $t = 5.670$ s, when the wavemaker is turned off. This net gain of energy occurs because the wavemaker leads to a net

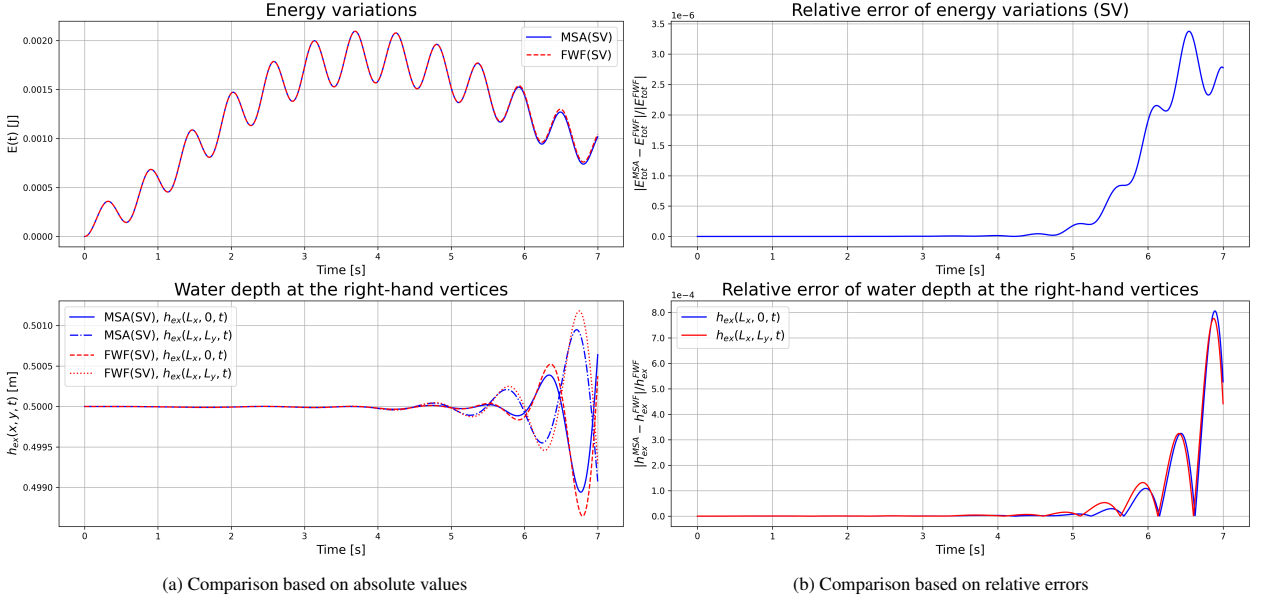


Fig. 6: Comparisons between TC2 and TC2b through energy variations (top row) and water depths $h_{ex}(L_x, 0, t)$ and $h_{ex}(L_x, L_y, t)$ (bottom row) based on (a) absolute values and (b) relative errors. Results obtained using spatial resolutions $\Delta y = \Delta x = 0.025\text{m}$ and the Störmer-Verlet scheme. Corresponding results based on the symplectic-Euler scheme are qualitatively and quantitatively similar. In (a), numerical results from TC2 (using MSA) are plotted in blue; those from TC2b (using FWF) are plotted in red.

energy input into the system, cf. definitions arising from (21) with (17), since

$$\frac{d(\mathcal{H} + \mathcal{R})}{dt} \neq 0. \quad (40)$$

Due to the wavemaker, the Hamiltonian depends explicitly on time. As a consequence the energy is not but the Kamiltonian is conserved, except when the wavemaker is turned off since then $\mathcal{R} = 0$ with $R(t) = 0$ such that also $d\mathcal{H}/dt = 0$. This is what is observed in Fig. 8, where no energy drift is observed after switching off the wavemaker (for $t > 5.670\text{s}$).

In Fig. 9, we verify the consistency of the temporal schemes by focussing on the energy variations after the wavemaker motion has been switched off (*i.e.*, for $5.670\text{s} \leq t \leq 17\text{s}$). The Hamiltonian dynamics of our temporal schemes result in bounded and small-amplitude energy oscillations. The amplitude of these oscillations diminishes for smaller time steps. With the symplectic-Euler scheme, variations ΔE_{SE} in the case SE2 are twice those for the case SE1, in-keeping with the theory underlying a first-order scheme, *i.e.*

$$\Delta E_{SE}(\Delta t_2) = 2\Delta E_{SE}(\Delta t_1), \quad \text{for } \Delta t_2 = 2\Delta t_1. \quad (41)$$

That is, the amplitude of the energy oscillations is doubled by doubling the time step. Similarly, for the second-order Störmer-Verlet scheme, energy variations ΔE_{SV} in case SV2 are four times larger than those in the case SV1:

$$\Delta E_{SV}(\Delta t_2) = 4\Delta E_{SV}(\Delta t_1), \quad \text{for } \Delta t_2 = 2\Delta t_1, \quad (42)$$

i.e., a quadratic increase of the energy oscillations accrues when doubling the time step.

In terms of computational time, the symplectic-Euler scheme is approximately twice as fast as the Störmer-Verlet scheme. On 16 cores, cases SE1 and SV1 ran in 1h47min and 3h44min respectively (*i.e.*, a 2.1 ratio), and cases SE2 and SV2 in 54min and 2h10min respectively (*i.e.*, a 2.4 ratio). However, the accuracy of the Störmer-Verlet scheme is higher than that of the symplectic-Euler scheme, since the error decreases quadratically with the time step. The vertical scales in Fig. 9 show that, for the same time step, the energy variations obtained with Störmer-Verlet are about 100 times smaller than those obtained with symplectic-Euler (order $O(10^{-6})$ vs order $O(10^{-4})$ respectively). Since symplectic-Euler is a first-order scheme, the time step would need to be 100 times smaller to get oscillations of order 10^{-6} and thus obtain the same accuracy as with Störmer-Verlet. Consequently, the computational time would

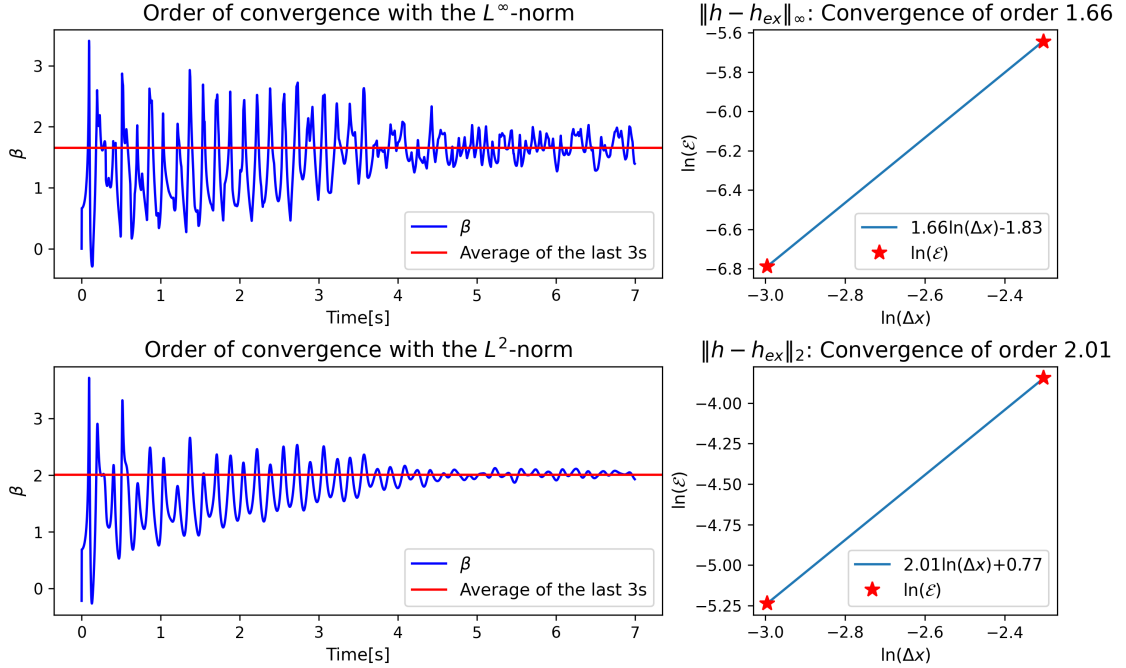


Fig. 7: TC2b: Temporal evolution of the spatial-convergence indices β characterized by L^∞ -norm (top row) and L^2 -norm (bottom row) based on results obtained from Störmer-Verlet scheme with full weak formulations.

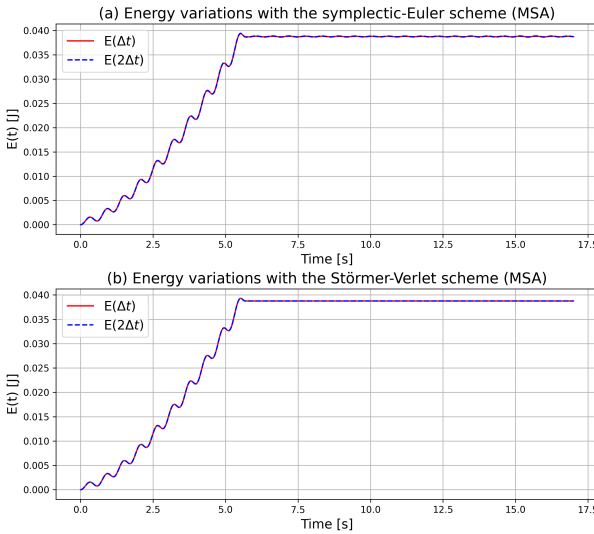


Fig. 8: TC3: Energy evolutions using the MSA in the (a) first-order symplectic-Euler and (b) second-order Störmer-Verlet schemes. The wavemaker generates the waves from $t = 0.0$ s to $t = 5.670$ s and is then turned off. The simulations are computed with $\Delta t_1 = 0.001$ s (continuous red line) and $\Delta t_2 = 2\Delta t_1 = 0.002$ s (dashed blue line).

be about 100 times longer, so the same accuracy is reached about 50 times faster with Störmer-Verlet than with symplectic Euler. One therefore needs to choose the time scheme carefully via a full consideration of the required objectives. If the objective is to limit computational time over the accuracy, then the symplectic-Euler scheme is a better option. However, if the objective is to minimise the error, then Störmer-Verlet is definitely the best choice.

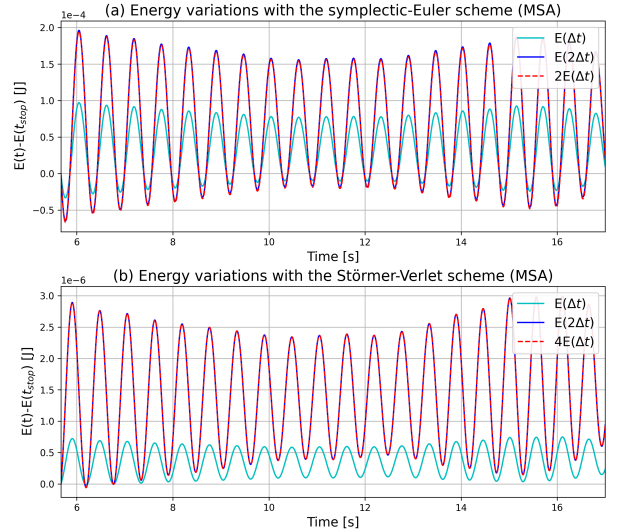


Fig. 9: TC3: Energy variations with (a) the first-order symplectic-Euler and (b) the second-order Störmer-Verlet schemes in the absence of wavemaker motion. Continuous cyan lines show variations in cases SE1 (a) and SV1 (b). Continuous blue lines show variations in cases SE2 (a) and SV2 (b), and the dashed red lines are respectively twice the variations of SE1 (a) and four times the variations of SV1 (b).

Domain				Beach	
L_x [m]	L_y [m]	H_0 [m]	$H(x = L_x)$ [m]	x_b [m]	s_b [-]
6.5	1.0	1.0	0.5	4.0	0.2
Wavemaker					
λ [m]	k [rad/m]	ω [rad/s]	T_w [s]	γ [m]	L_w [m]
2.0	3.14	5.54	1.13	0.03	1.0
Resolution					
Δx [m]	Δy [m]	N_{xy} [-]	N_z [-]	Δt_1 [s]	Δt_2 [s]
0.05	0.05	2751	9	0.001	0.002

Table 2: Parameters used in TC3. Dimensions are given in square brackets. Each simulation runs from $t = 0$ s to $t = t_{\text{end}} = 17$ s and the wavemaker is turned off at $t = t_{\text{stop}} = 5.670$ s.

4.2.4. TC3b: Energy conservation and temporal convergence without the mild-slope approximation

For TC3b, we reuse all parameters from TC3 but now remove the MSA, thereby using full energy expressions and full weak formulations. The comparisons between this pair of test cases for the symplectic-Euler scheme with time resolution Δt_2 are shown in Fig. 10. It can be seen from the figure that, similar to Fig. 6, the MSA has only a minor effect on the energy variations: as the Fig. 10 insets show, any differences in the results are noticeable on only an expanded scale after the wavemaker stops, when the relative errors for both the symplectic-Euler and Störmer-Verlet schemes reach their maxima with orders $O(10^{-6})$ and $O(10^{-8})$ respectively. Fig. 10 reveals similar small relative differences (for both schemes, $< 4\%$) in the amplitudes of the water depths computed at the right-hand vertices of the computational domain, where $b(x)$ reaches its maximum value $s_b(L_x - x_b)$. In contrast with the minor differences in energy variations, these differences are more pronounced after the wavemaker stops; this larger relative discrepancy can be interpreted as resulting from (a) waves with higher amplitudes being formed by the larger-amplitude wavemaker oscillation ($\gamma = 0.03$ in TC3/TC3b whereas $\gamma = 0.02$ in TC2/TC2b); (b) waves travelling longer distances towards the right-hand boundary entering a region of gradually decreasing depth due to the upwardly sloping bed ($L_x = 6.5$ m vs $L_x = 4$ m); (c) the simulations occurring over a longer time-period ($T_{\text{end}} = 17$ s vs $T_{\text{end}} = 7$ s).

Similarly, as confirmed by comparisons between energy variations in TC3b computed with two time resolutions—which are shown Fig. 11 and Fig. 12—the conclusions drawn from TC3 concur fully with those drawn from TC3b, in that the energy shows bounded oscillations and no drift after the wavemaker stops. Furthermore, the consistencies of the two schemes are again verified based on the linear and quadratic increase of the amplitudes of energy variations when doubling the time resolution.

4.3. TC4: Validation against wavetank data

Experiments were conducted in the shallow-water basin of MARIN (cf. test case 202002 in [22]), which includes piston wavemakers and a flat bottom, with a rest depth of $H(x) = H_0 = 1.0$ m, cf. Fig. 13. Several wave groups of various steepness were generated in order to generate a focussed wave. Probes were placed at various locations $x_1 = 10$ m, $x_2 = 20$ m, $x_3 = 40$ m, $x_4 = 49.5$ m, $x_5 = 50$ m and $x_6 = 54$ m from the wavemaker in order to measure the free-surface elevation. These data as well as the wavemaker motion and velocity were recorded at a frequency of 50Hz and used to initialise and validate our numerical model in a two-dimensional vertical plane, cf. [8].

4.3.1. Importing data from measurements

In order to generate the same wave spectra as those in the shallow-water basin of MARIN, the measured wavemaker motion and velocity are interpolated linearly and assigned to the corresponding numerical functions at each time step. To meet the CFL condition (33), the time step Δt used in our simulations must be smaller than the one used to record the data, i.e. $\Delta t_{\text{data}} = 1/50$ s. To use the measured wavemaker motion and velocity at each time step, we interpolate them with first-order polynomials in each measured time interval $[t_1, t_2]$. Therefore, at time t , the interpolated motion $R_{\text{int}}(t)$ and velocity $u_{\text{int}}(t)$ of the measured motion R_{dat} and measured velocity u_{dat} are obtained as

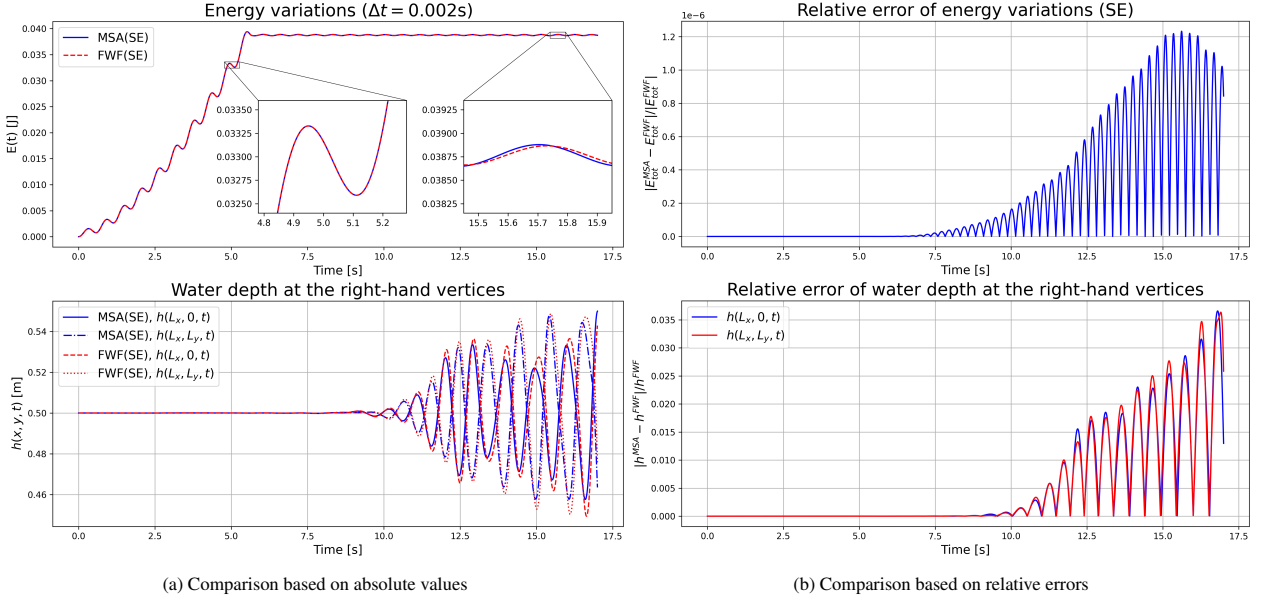


Fig. 10: Comparisons between TC3 and TC3b through energy variations (top row) and water depths $h(L_x, 0, t)$ and $h(L_x, L_y, t)$ (bottom row) based on (a) absolute values and (b) relative errors. Results obtained using time resolution $\Delta t_2 = 0.002s$ and the symplectic-Euler scheme. Corresponding results based on the Störmer-Verlet scheme for water depths are quantitatively similar, whereas the relative error for the energy variations is smaller (of the order $O(10^{-8})$). In (a), numerical results from TC3 (using MSA) are plotted in blue; those from TC3b (using FWF) are plotted in red.

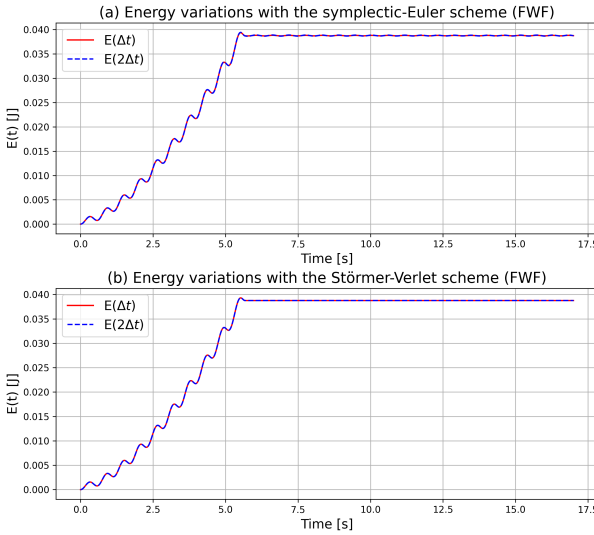


Fig. 11: TC3b: Energy evolutions with (a) first-order symplectic-Euler and (b) second-order Störmer-Verlet schemes by using full energy expressions and full weak formulations (FWF). The wavemaker generates the waves from $t = 0.0s$ to $t = 5.670s$ and is then turned off. The simulations are computed with $\Delta t_1 = 0.001s$ (continuous red line) and $\Delta t_2 = 2\Delta t_1 = 0.002s$ (dashed blue line).

follows

$$R_{int}(t) = \frac{(t - t_1)R_{dat}(t_2) - (t - t_2)R_{dat}(t_1)}{t_2 - t_1} \quad \text{and} \quad u_{int}(t) = \frac{(t - t_1)u_{dat}(t_2) - (t - t_2)u_{dat}(t_1)}{t_2 - t_1}. \quad (43)$$

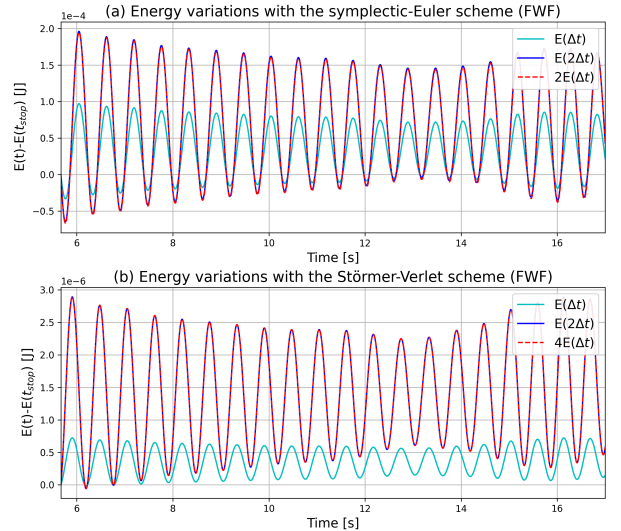


Fig. 12: TC3b: Energy variations with (a) the first-order symplectic-Euler and (b) the second-order Störmer-Verlet schemes in the absence of wavemaker motion. The continuous cyan lines show variations in the cases SE1 (a) and SV1 (b). The continuous blue lines show variations in the cases SE2 (a) and SV2 (b), and the dashed red lines are respectively twice the variations of SE1 (a) and four times the variations of SV1 (b).

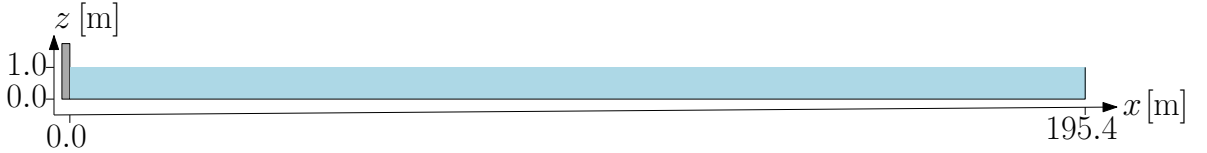


Fig. 13: TC4: schematic of MARIN's wave basin. The tank is 195.4m long, with a constant water depth at rest of 1.0m. A piston-type wavemaker oscillates sinusoidally with mean position $x = 0\text{m}$ and generates the waves.

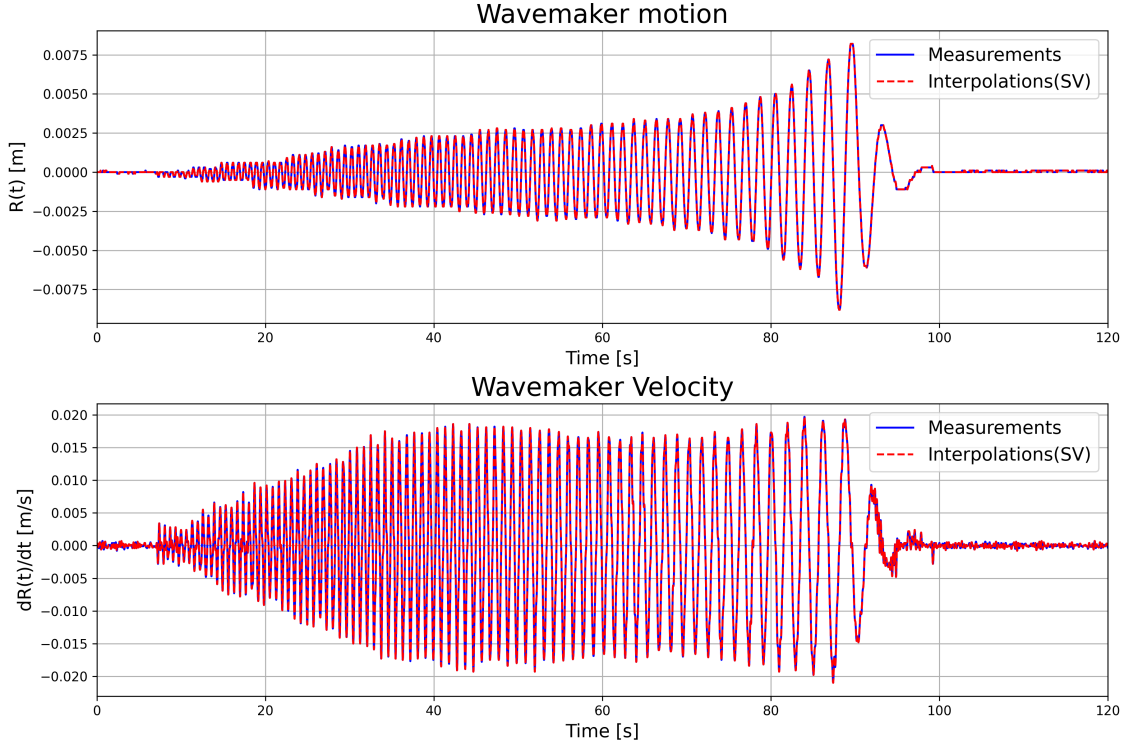


Fig. 14: TC4: Interpolated and measured wavemaker motion (top) and velocity (bottom) in the case of focussed wave generation.

The interpolations (43) are updated in time and numerically assigned to the wavemaker motion and velocity functions. Note that we consider 2D vertical waves, whence there is no y -dependence in the wavemaker motion, i.e., $\partial_y R = 0$. Fig. 14 shows that the interpolated motion and velocity of the wavemaker agrees with the measurements to a degree that is visually indistinguishable on the presented scale (i.e. approximately 10^{-3} relative error). The numerical free-surface elevation resulting from this wavemaker input signal may then be saved and compared to the experimental data. Simulations are analysed in the next section.

4.3.2. Focussed wave: dispersion effects

The wavemaker input is used to simulate a focussed wave. The wavemaker starts at rest and oscillates with varying amplitude and anharmonic frequencies (*cf.* Fig. 14). Due to dispersion, the waves generated later are longer and hence travel faster than the first waves, such that waves focus at a specific position. In order to capture this wave focussing, probes are placed around a target area near $x = 49.5\text{m}$ and $x = 50\text{m}$.

We consider a 100m-long computational basin with flat seabed (i.e., $b(x, y) = 0$) and rest water depth $H(x, y) = H_0 = 1.0\text{m}$. A fast Fourier transform of the measured wave signals (*cf.* Fig. 18) shows that the maximal relevant frequency is about $\omega \approx 18\text{Hz}$. The shortest wavelength may thus be estimated from the linear dispersion relation (35c) with $k = 2\pi/\lambda$, leading to $\lambda \approx 0.19\text{m}$. Hence, *cf.* (33), stability requires $\Delta x \leq \lambda$, so that the full length of the wave can be resolved by the mesh. However, to ensure accurate results, the wavelength should be evaluated over more than one finite element. To increase numerical accuracy, the mesh resolution is set to $\Delta x = \min \lambda/20 = 0.01\text{m}$

and, as a consequence, the time step must satisfy

$$\Delta t \leq \frac{2}{\sqrt{g(2\pi/\Delta x) \tanh(2\pi H_0/\Delta x)}} = 0.025\text{s}. \quad (44)$$

To increase accuracy, we set $\Delta t = \max \Delta t / 20 = 0.001\text{s}$, cf. the time step used in [8]. Finally, the depth is split into nine horizontal layers ($\Delta z = 0.125\text{m}$), meaning that the system comprises, in addition to the depth h , nine unknowns for the velocity potentials (ψ_1 at the surface and $\psi_{2,\dots,9}$ in the interior).

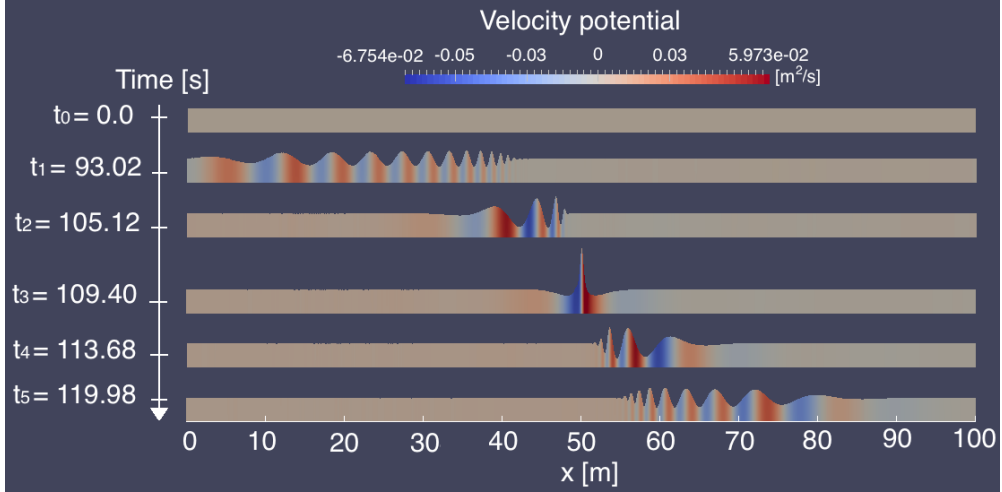


Fig. 15: TC4: Temporal snapshots of the velocity potential at times $t_0 = 0.0\text{s}$, $t_1 = 93.01\text{s}$, $t_2 = 105.12\text{s}$, $t_3 = 109.40\text{s}$, $t_4 = 113.68\text{s}$ and $t_5 = 119.98\text{s}$. The focussed wave is captured at time $t_3 = 109.40\text{s}$.

Figs. 15 and 16 show snapshots of the velocity potential and free-surface elevation respectively, obtained with the symplectic-Euler scheme. First, from $t_0 = 0.0\text{s}$ to $t_1 = 93.02\text{s}$, waves with increasing length and amplitude are generated. At time $t_2 = 105.12\text{s}$, it is evident that the waves are closer to each other than when initially generated: dispersion causes the longer waves to travel faster than the shorter ones. At time $t_3 = 109.40\text{s}$, the longest waves have caught up with the first, shorter ones, forming a “freak wave” whose amplitude is more than five times higher than waves generated at the early stage of the experiment. Immediately after time t_3 , the longest, fastest waves overtake the shortest ones (*e.g.* at times $t_4 = 113.68\text{s}$ and $t_5 = 119.98\text{s}$), and the waves split again, leading to a mirror-configuration relative to the focussed wave, *i.e.*, compare the snapshot at time t_2 with the one at time t_4 .

Fig. 17 compares the measured (red) time evolution of the wave elevation at the probes with the numerical evolution obtained for the symplectic-Euler (dark blue) and Störmer-Verlet (cyan) schemes. Both schemes agree reasonably well with the measurements. The freak-wave phase and location agree with the measurements for simulated waves in a target area at least 50m from the wavemaker. Using frequency spectra, Fig. 18 shows that all the experimental modes are well-captured by the present numerical model. In addition, numerical results obtained from the symplectic-Euler scheme agree well with those in [8], as demonstrated in Fig. 18.

5. Summary and discussion

A methodology has been developed for the modelling and subsequent computational solution of three-dimensional nonlinear potential-flow problems. The new approach has been demonstrated to overcome the following four industrial and computational challenges.

First, we have checked the model **accuracy** through validation against data of past experiments undertaken at MARIN. The simulations not only show good agreement with the measurements but also manage to capture the extreme, freak-wave elevation. The model thus enables the simulation of the nonlinear free surface between water and air, as required in many maritime applications. For example, future applications can include the improvement of previous simulations of wave propagation in a Hele-Shaw cell [31] by replacing the shallow-water waves with

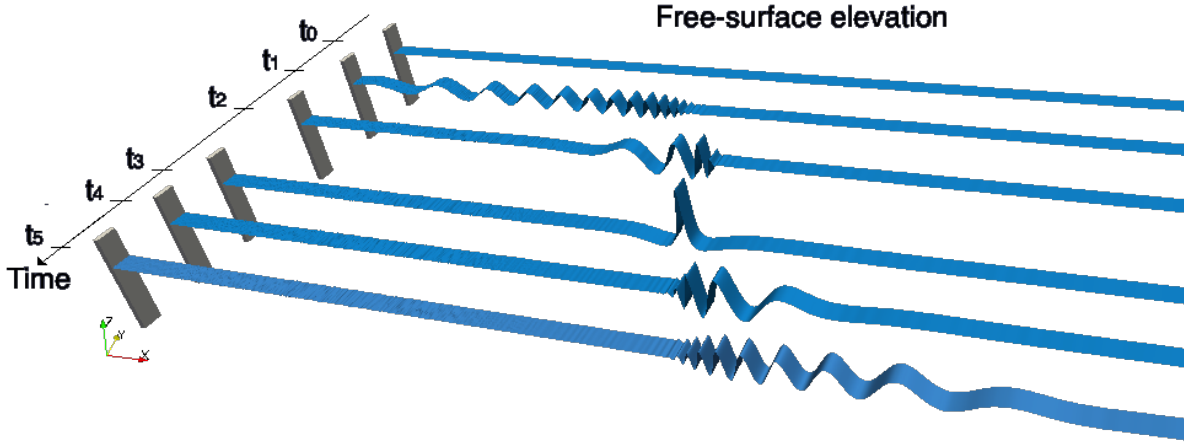


Fig. 16: TC4: Temporal snapshots of the free-surface elevation, each rendered as a 3D ribbon, at times $t_0 = 0.0\text{s}$, $t_1 = 93.01\text{s}$, $t_2 = 105.12\text{s}$, $t_3 = 109.40\text{s}$, $t_4 = 113.68\text{s}$ and $t_5 = 119.98\text{s}$. The focussed wave is captured at time $t_3 = 109.40\text{s}$, whereafter the wave is defocussing again.

nonlinear potential-flow waves. The model can also be used to accurately predict the location of a freak wave and its impact on marine structures that may be placed in wave basins for testing.

Second, the variational approach has ensured **stability** of the simulations, both in non-autonomous and autonomous cases. In the former, the energy of the wavemaker is accurately transferred to the waves. In the latter case, when the wavemaker is turned off, the overall energy-oscillations are bounded with a small amplitude that decreases with the time step. Consequently, simulations of extreme waves are stable, thereby enabling a better analysis of the wave loads on marine structures.

Third, both model and discretization methods were designed to be easily usable and hence readily adaptable to diverse applications, thus offering **flexibility** on many fronts. The user can change the type of finite-element expansions in the horizontal direction — Firedrake offers a wide range of possibilities such as Galerkin, Lagrange *etc.* — and in the vertical direction — the Lagrange interpolation (10) may be replaced by any other polynomials, such as a spline interpolation. Additionally, the distribution of the vertical extension — the linear expansion (11) — may for example be replaced by an exponential distribution. The length of the domain to transform in x may also be adapted by changing the wavemaker part of the domain specified via L_w , *etc.* Moreover, the comparison between the first-order symplectic-Euler and second-order Störmer-Verlet time-integration schemes assists the user in an optimal choice of a temporal discretization: while the Störmer-Verlet scheme minimizes the numerical error, it is also more time-consuming than the symplectic-Euler scheme and hence the choice to be considered is one of optimising either computational speed or accuracy. Other higher-order schemes, such as the third-order scheme obtained variationally in [16] may be implemented and explored.

Finally, Firedrake codes can be run in parallel using P processes through an MPI call:

```
mpicexec -n P python3 3D_tank.py
```

which, for a large number of elements (> 10000), will increase the **computational speed**. The present model may be used to optimise larger, industrial-scale maritime simulations, thereby saving computational resources and enhancing the overall project efficiency and quality. Possible extensions are presented next.

5.1. Extension to wave-structure interactions

In section 4.3.2, a freak wave was generated at a specific location in the basin. More generally, the fast computational speed of the model enables the tuning of the wavemaker motion in order to adjust the location of the freak wave. Placing a maritime structure in the target area, both in the numerical and experimental wave tanks, will enable measurement of the wave's impact upon a vessel or a wind turbine in order to assist engineers in the design of more robust structures. Our discretization strategies were designed with future extension to wave-structure interactions in mind. The restriction of the x -transform to the region nearest to the wavemaker allows any marine structure to be placed in the wave tank without needing to make additional, geometrically bespoke transforms in that region.

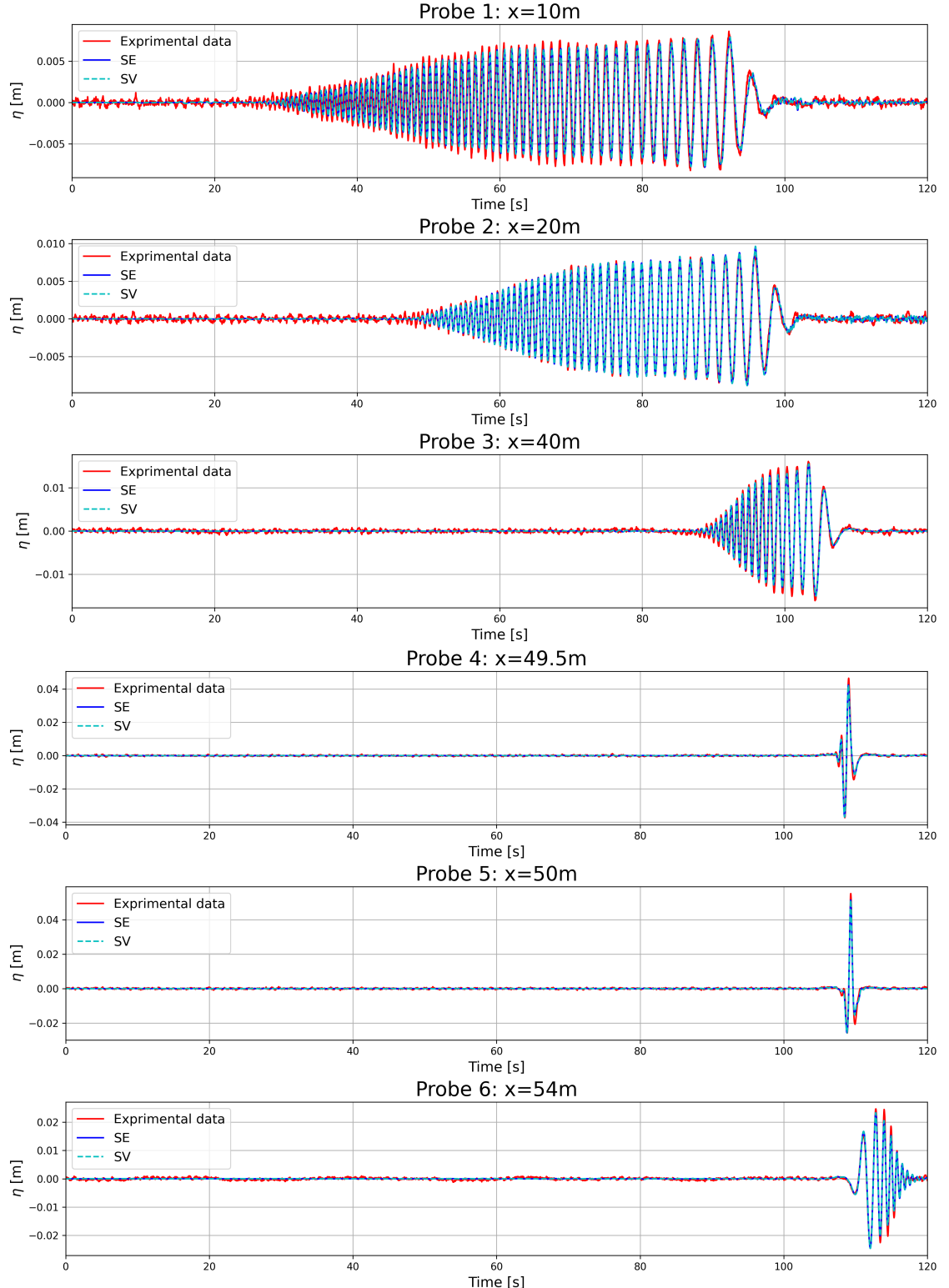


Fig. 17: TC4: wave elevations of numerical (blue and cyan) and experimental (red) data at various locations. Numerical results are obtained with the symplectic-Euler (blue continuous line) and the Störmer-Verlet (cyan dashed line) schemes.

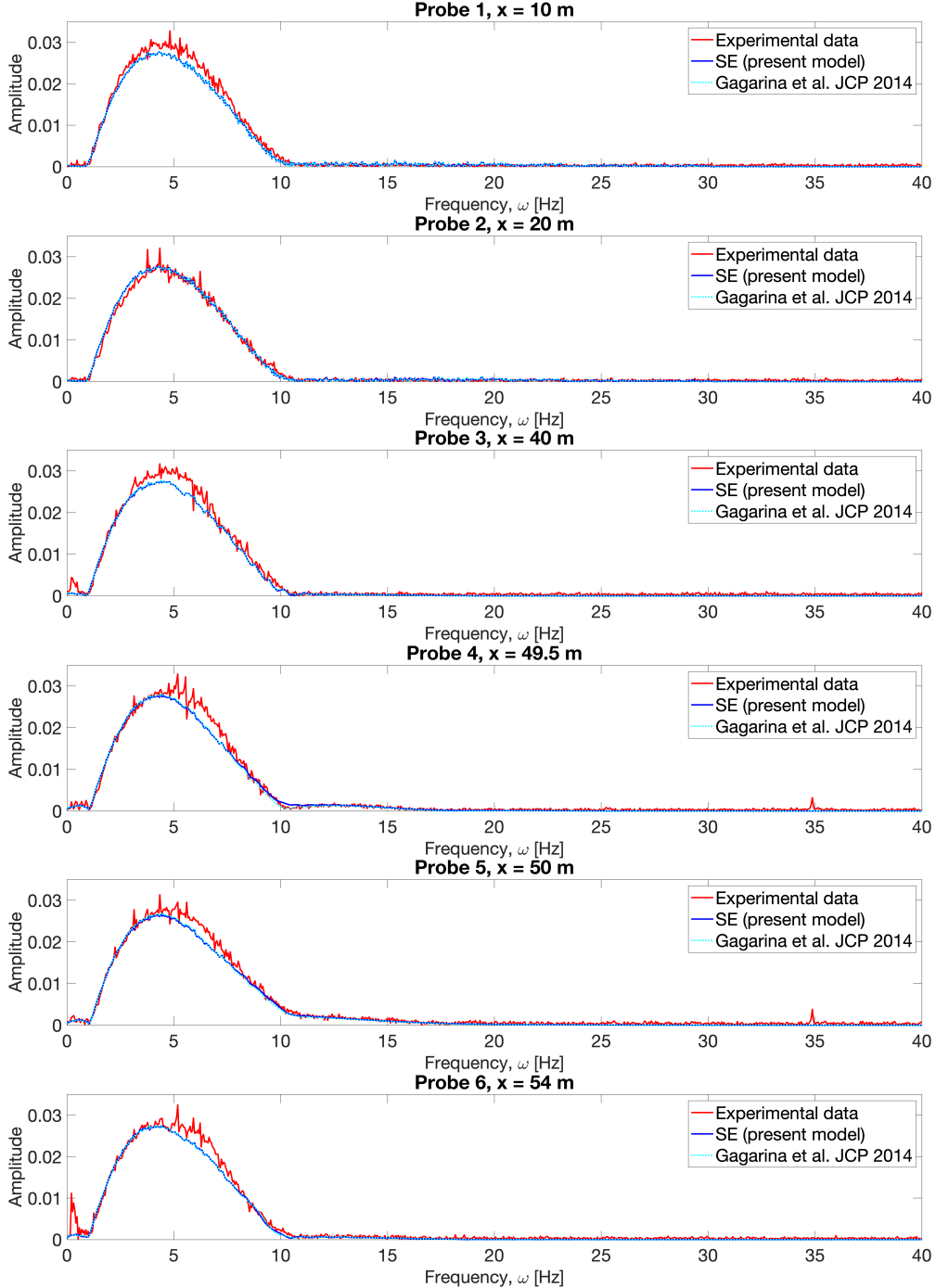


Fig. 18: TC4: fast Fourier transform of the wave elevations of numerical (blue and cyan) and experimental (red) data at various locations. Numerical results including these obtained from the present model with symplectic-Euler scheme (blue continuous line) and others from the same test performed in [8] (cyan dashed-dotted line).

5.2. Three-dimensional rogue-type wave simulations

The ability of our model to simulate three-dimensional rogue-type waves can be explored further. First, the configuration used in [32] to simulate solitary-wave interaction with an oblique wall can be extended by replacing the Benney-Luke model used therein by a nonlinear potential-flow model. This extension may require the derivation of a soliton solution for the nonlinear potential-flow equation, within the realm of Miles' theory, or by imposing a

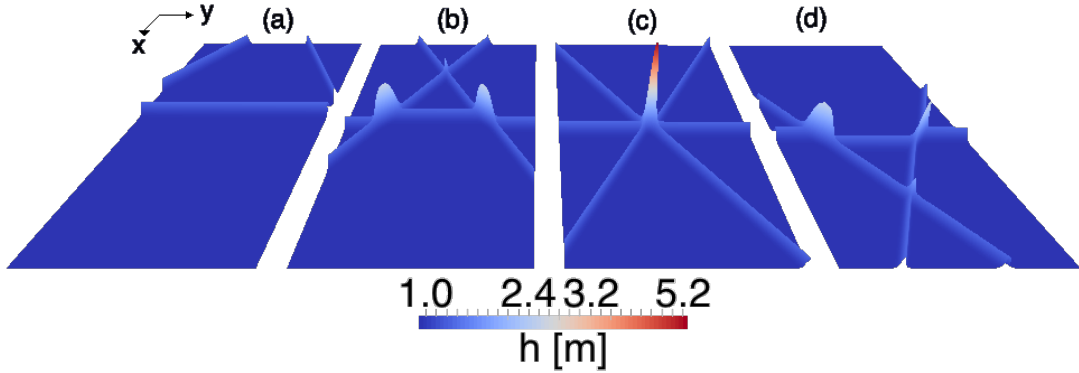


Fig. 19: Analytical solution of a circa ninefold amplification resulting from the interaction of three solitons, derived in Baker [33]. (a): Three initial solitons travel in the positive x -direction, with amplitude $A_0 = 0.5$. (b): Two-by-two soliton interactions. (c): The three solitons interact, leading to a wave of maximum amplitude $A = 4.2 = 8.4A_0$. (d): Undisturbed solitons continue to propagate with their initial angle and amplitude.

solution of the KdV-equation as initial condition. Another test case, based on the interaction of three solitons, can be investigated (*cf.* Fig. 19). Baker [33] derived an analytical solution based on the KP equation that may be used as approximate initial solution, of the present potential-flow model, in the computational quest for the “ultimate-rogue-wave” (nearly nine-fold) wave amplification. Test cases considering 3D high-amplitude rogue waves arising from the interactions of both two and three solitons are currently under development, as inspired by recent work [34] on two- and three-soliton interactions in which theoretical fourfold and ninefold amplifications are approximately captured by initializing the Benney-Luke system with exact two- and three-soliton solutions of the KP equation. In addition, in the presented potential-flow model, the free surface is represented by a single-valued function, therefore it cannot describe breaking waves when the wave slope becomes too steep. To address this challenge, we are going to introduce the wave-breaking model proposed in [35], where a viscous damping term is added to the free-surface kinematic and dynamic boundary conditions locally around the breaking region so that steep and breaking waves are parameterised in a sustainable simulation.

5.3. Extension to more sophisticated wave tanks

The discretization and implementation strategies derived and tested herein may be used to develop more sophisticated wave tanks, as follows.

Flap-type wavemaker: In the linear limit, fluid particles under deep-water waves follow a circular motion whose radius decreases with increasing depth. To mimic this fluid motion, many experimental wave tanks generate the waves via flap-type wavemakers; that is, wavemakers pivoting around their base within a symmetric wedge of angle α on either side of the initial vertical position. Extending the current piston wavemaker to a flap-type wavemaker may be achieved by extending the modelling strategies, discretization techniques and implementation method presented here.

Optimised wavemaker motions: Large-scale experimental wave tanks, such as those in MARIN, sometimes contain an additional wall with wavemakers in order to generate waves in multiple directions. Following the methodology developed, the present model can be extended with an additional wavemaker around the wall $y = 0$, to reproduce oblique wave motions, *cf.* Fig. 20.

Wave absorption at the beach: After reflection at the wall $x = L_x$, the waves travel back into the deep-water domain and adversely affect the target (experimental or simulation) area. Within the current model, the only way to limit disturbance of the target area by reflected waves is to increase the length of the domain so that the waves take more time to travel back to the deep-water area. This method is of course not optimal as it increases the computational time. A wave-absorbing boundary is thus required to reduce wave reflection without increasing the computation time. This can be done by coupling the current model to a sloping beach, partially wet and dry, with a moving dry-wet boundary, on which the waves will break and lose energy, *cf.* [29]. The addition of a beach with shallow-water wave breaking leads to new implementational constraints: it will result in a complete numerical wave tank simulating the generation, dynamics and absorption of the waves.

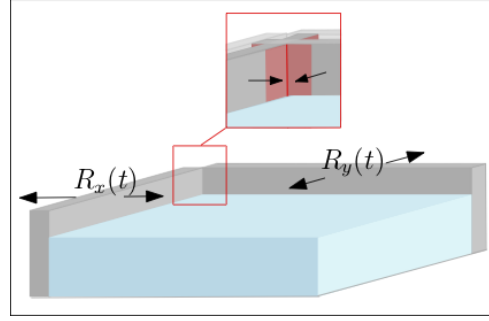


Fig. 20: Experimental tank with wavemakers on two sides, moving in such away that a collision is avoided in the corner (red).

Acknowledgments

This work was funded through an EU Marie Curie Fellowship for European Industry Doctorates within the projects “SurfUp” and “EAGRE”(project number GA 859983). Dr Elena Gagarina kindly provided her Fourier-analysis code and the resulting data from her simulations [8]. The original formulation and codes were developed by FG [29]; OB and MK further checked and improved the formulations and write-ups of both the mathematical analysis and numerical model; following updates of Firedrake, models and codes were again improved and verified, and then reproduced/extended by YL, who: found and corrected an error (identified earlier as model error by OB and MAK but not fully corrected) in both model and code in [29], including optimisation and entirely re-coding all weak formulations, implemented inclusion/testing of the option to toggle the mild-slope approximation on and off, and; the established simulation and analysis instructions on GitHub, thus ensuring reproducibility [36]; both FG and YL were supervised throughout by OB and MK. Codes used and corresponding simulation set-ups can be found at <https://github.com/EAGRE-water-wave-impact-modelling/3D-wave-tank-JCP2022> and www.zenodo.org (link to be added later).

Appendix A. Coordinate transformation

The Jacobian of transforms (4) mapping (x, y, z, t) to $(\hat{x}, \hat{y}, \hat{z}, \hat{t})$ is, after substitution of all *explicit* occurrences of x , y , z and t ,

$$J \equiv \frac{\partial(\hat{x}, \hat{y}, \hat{z}, \hat{t})}{\partial(x, y, z, t)} = \begin{bmatrix} \frac{L_w}{L_w - \tilde{R}} & \frac{(\hat{x} - L_w)\tilde{R}_y}{L_w - \tilde{R}} & 0 & \frac{(\hat{x} - L_w)\tilde{R}_t}{L_w - \tilde{R}} \\ 0 & 1 & 0 & 0 \\ -\frac{\hat{z}h_x + H_0b_x}{h} & -\frac{\hat{z}h_y + H_0b_y}{h} & \frac{H_0}{h} & -\frac{\hat{z}h_t}{h} \\ 0 & 0 & 0 & 1 \end{bmatrix}, \quad (\text{A.1})$$

in which partial derivatives with respect to x, y, t must now be expressed explicitly in terms of transformed variables. To this end, first note that the inverse

$$\hat{J} \equiv \frac{\partial(x, y, z, t)}{\partial(\hat{x}, \hat{y}, \hat{z}, \hat{t})}$$

of J is computed directly from (A.1) as

$$\hat{J} = \begin{bmatrix} \frac{L_w - \tilde{R}}{L_w} & -\frac{(\hat{x} - L_w)\tilde{R}_y}{L_w} & 0 & -\frac{(\hat{x} - L_w)\tilde{R}_t}{L_w} \\ 0 & 1 & 0 & 0 \\ \frac{(\hat{z}h_x + H_0b_x)(L_w - \tilde{R})}{L_w H_0} & \frac{\hat{z}h_y + b_y - \frac{(\hat{z}h_x + H_0b_x)(\hat{x} - L_w)\tilde{R}_y}{L_w H_0}}{H_0} & \frac{h}{H_0} & \frac{\hat{z}h_t - \frac{(\hat{z}h_x + H_0b_x)(\hat{x} - L_w)\tilde{R}_t}{L_w H_0}}{H_0} \\ 0 & 0 & 0 & 1 \end{bmatrix}, \quad (\text{A.2})$$

whence the chain rule and (A.2) give

$$\begin{bmatrix} b_z \\ h_z \\ \tilde{R}_z \end{bmatrix} = \underline{\hat{J}_{1,3}} \begin{bmatrix} b_x \\ h_x \\ \tilde{R}_x \end{bmatrix} + \underline{\hat{J}_{2,3}} \begin{bmatrix} b_y \\ h_y \\ \tilde{R}_y \end{bmatrix} + \underline{\hat{J}_{3,3}} \begin{bmatrix} b_z \\ \underline{h_z} \\ \underline{\tilde{R}_z} \end{bmatrix} + \underline{\hat{J}_{4,3}} \begin{bmatrix} b_t \\ h_t \\ \tilde{R}_t \end{bmatrix} = \begin{bmatrix} 0 \\ 0 \\ 0 \end{bmatrix}. \quad (\text{A.3})$$

in which singly and doubly underlined terms vanish by (4) and (A.2) respectively. Applying the chain rule once again now gives

$$\begin{bmatrix} \tilde{R}_y \\ \tilde{R}_t \end{bmatrix} = \begin{bmatrix} J_{1,2} \\ J_{1,4} \end{bmatrix} \underline{\tilde{R}_{\hat{x}}} + \begin{bmatrix} J_{2,2} \\ \underline{J_{2,4}} \end{bmatrix} \tilde{R}_{\hat{y}} + \begin{bmatrix} J_{3,2} \\ J_{3,4} \end{bmatrix} \underline{\tilde{R}_{\hat{z}}} + \begin{bmatrix} J_{4,2} \\ \underline{J_{4,4}} \end{bmatrix} \tilde{R}_{\hat{t}} = \begin{bmatrix} 1 \\ 0 \end{bmatrix} \tilde{R}_{\hat{y}} + \begin{bmatrix} 0 \\ 1 \end{bmatrix} \tilde{R}_{\hat{t}} = \begin{bmatrix} \tilde{R}_{\hat{y}} \\ \tilde{R}_{\hat{t}} \end{bmatrix}, \quad (\text{A.4a})$$

$$\begin{bmatrix} b_x \\ b_y \end{bmatrix} = \begin{bmatrix} J_{1,1} \\ J_{1,2} \end{bmatrix} b_{\hat{x}} + \begin{bmatrix} J_{2,1} \\ \underline{J_{2,2}} \end{bmatrix} b_{\hat{y}} + \begin{bmatrix} J_{3,1} \\ J_{3,2} \end{bmatrix} \underline{b_{\hat{z}}} + \begin{bmatrix} J_{4,1} \\ \underline{J_{4,2}} \end{bmatrix} b_{\hat{t}} = \frac{1}{\hat{W}} \begin{bmatrix} L_w \\ \hat{U} \end{bmatrix} b_{\hat{x}} + \begin{bmatrix} 0 \\ 1 \end{bmatrix} b_{\hat{y}}, \quad (\text{A.4b})$$

$$\begin{bmatrix} h_x \\ h_y \\ h_t \end{bmatrix} = \begin{bmatrix} J_{1,1} \\ J_{1,2} \\ J_{1,4} \end{bmatrix} h_{\hat{x}} + \begin{bmatrix} J_{2,1} \\ \underline{J_{2,2}} \\ \underline{J_{2,4}} \end{bmatrix} h_{\hat{y}} + \begin{bmatrix} J_{3,1} \\ J_{3,2} \\ J_{3,4} \end{bmatrix} \underline{h_{\hat{z}}} + \begin{bmatrix} J_{4,1} \\ \underline{J_{4,2}} \\ \underline{J_{4,4}} \end{bmatrix} h_{\hat{t}} = \frac{1}{\hat{W}} \begin{bmatrix} L_w \\ \hat{U} \\ \hat{X} \tilde{R}_{\hat{t}} \end{bmatrix} h_{\hat{x}} + \begin{bmatrix} 0 \\ 1 \\ 0 \end{bmatrix} h_{\hat{y}} + \begin{bmatrix} 0 \\ 0 \\ 1 \end{bmatrix} h_{\hat{t}} \quad (\text{A.4c})$$

\tilde{R} is the same expression (5) for either hatted or plain variables. Its derivative is a delta function in both cases. I suppose that delta function always has support zero at L_w , i.e. since $J_{1,2}, J_{1,4}$ are zero at L_w so under any integral in x these terms disappear as they should. But it all becomes mathematical navel-gazing since using the Heaviside function is simply used to glue to separate domains together for which there cannot be a contribution at L_w , in which singly, doubly and triply underlined terms vanish by (4), (A.1) and (A.3) respectively, and where \hat{X} , \hat{U} and \hat{W} are defined in (7), in which hats were hitherto removed for brevity but now resurrected to distinguish between coordinate systems. Substitution of (A.4) into (A.1) now leads to the fully explicit form of the required Jacobian,

$$J = \begin{bmatrix} \frac{L_w}{\hat{W}} & \frac{\hat{U}}{\hat{W}} & 0 & \frac{\hat{X}}{\hat{W}} \tilde{R}_{\hat{t}} \\ 0 & 1 & 0 & 0 \\ -\frac{L_w \hat{z} h_{\hat{x}} + H_0 b_{\hat{x}}}{h} & -\frac{\hat{z}}{h} \left(\frac{\hat{U}}{\hat{W}} h_{\hat{x}} + h_{\hat{y}} \right) - \frac{H_0}{h} \left(\frac{\hat{U}}{\hat{W}} b_{\hat{x}} + b_{\hat{y}} \right) & \frac{H_0}{h} & -\frac{\hat{z}}{h} \left(\frac{\hat{X}}{\hat{W}} \tilde{R}_{\hat{t}} h_{\hat{x}} + h_{\hat{t}} \right) \\ 0 & 0 & 0 & 1 \end{bmatrix}, \quad (\text{A.5})$$

using which the required transformed partial derivatives of the potential ϕ follow from the chain rule and (A.5) as

$$\begin{bmatrix} \phi_x \\ \phi_y \\ \phi_z \\ \phi_t \end{bmatrix} = J^T \begin{bmatrix} \phi_{\hat{x}} \\ \phi_{\hat{y}} \\ \phi_{\hat{z}} \\ \phi_{\hat{t}} \end{bmatrix} = \frac{1}{\hat{W}} \begin{bmatrix} L_w \\ \hat{U} \\ 0 \\ \hat{X} \tilde{R}_{\hat{t}} \end{bmatrix} \phi_{\hat{x}} + \begin{bmatrix} 0 \\ 1 \\ 0 \\ 0 \end{bmatrix} \phi_{\hat{y}} - \frac{1}{\hat{W} h} \begin{bmatrix} L_w (\hat{z} h_{\hat{x}} + H_0 b_{\hat{x}}) \\ \hat{U} (\hat{z} h_{\hat{x}} + H_0 b_{\hat{x}}) + \hat{W} (\hat{z} h_{\hat{y}} + H_0 b_{\hat{y}}) \\ -\hat{W} H_0 \\ \hat{z} (\hat{X} \tilde{R}_{\hat{t}} h_{\hat{x}} + \hat{W} h_{\hat{t}}) \end{bmatrix} \phi_{\hat{z}} + \begin{bmatrix} 0 \\ 0 \\ 0 \\ 1 \end{bmatrix} \phi_{\hat{t}}. \quad (\text{A.6})$$

Finally, the spatio-temporal volume element in (2) transforms according to

$$dx dy dz dt = |\hat{J}| d\hat{x} d\hat{y} d\hat{z} d\hat{t} = \frac{\hat{W}}{L_w} \frac{h}{H_0} d\hat{x} d\hat{y} d\hat{z} d\hat{t}. \quad (\text{A.7})$$

Appendix B. Transformed z -discrete weak formulations

Variations of (17) with respect to h lead to the following weak formulation for the temporal variation of surface potential ψ_1 :

$$\begin{aligned} \int_0^T \int_{\hat{\Omega}_{x,y}} H_0 \partial_t (W\psi_1) \delta h \, dx \, dy \, dt &= - \int_0^T \left\{ \int_{\hat{\Omega}_{x,y}} \left[\frac{\delta h}{2} \left(\tilde{M}_{11} \bar{\nabla}(\psi_1, \psi_1) + 2\psi_{1,x} \tilde{M}_{1N}^T \left(\frac{V}{W} \hat{\psi}_x + U \hat{\psi}_y \right) \right. \right. \right. \\ &\quad \left. \left. \left. + 2\psi_{1,y} \tilde{M}_{1N}^T \left(U \hat{\psi}_x + W \hat{\psi}_y \right) + \frac{V}{W} \hat{\psi}_x^T \tilde{M}_{NN} \hat{\psi}_x + 2U \hat{\psi}_x^T \tilde{M}_{NN} \hat{\psi}_y + W \hat{\psi}_y^T \tilde{M}_{NN} \hat{\psi}_y \right) \right. \right. \\ &\quad \left. \left. \left. + \frac{1}{h} \left(\psi_1 \tilde{S}_{11} \psi_1 + 2\psi_1 \tilde{S}_{1N}^T \hat{\psi} + \hat{\psi}^T \tilde{S}_{NN} \hat{\psi} \right) \left(\bar{\nabla}(h, \delta h) - \frac{\delta h}{2h} \bar{\nabla}(h, h) \right) \right. \right. \\ &\quad \left. \left. \left. - \frac{H_0^2}{2h^2} \delta h \left(\psi_1 \tilde{A}_{11} \psi_1 + 2\psi_1 \tilde{A}_{1N}^T \hat{\psi} + \hat{\psi}^T \tilde{A}_{NN} \hat{\psi} \right) \left(\bar{\nabla}(b, b) + W \right) \right. \right. \\ &\quad \left. \left. \left. + \frac{H_0}{h} \left(\psi_1 \tilde{C}_{11} \psi_1 + 2\psi_1 \tilde{C}_{1N}^T \hat{\psi} + \hat{\psi}^T \tilde{C}_{NN} \hat{\psi} \right) \left(\bar{\nabla}(b, \delta h) - \frac{\delta h}{h} \bar{\nabla}(b, h) \right) \right. \right. \\ &\quad \left. \left. \left. - \left(\left(\bar{\nabla}(\delta h, \psi_1) \tilde{D}_{11} + \bar{\nabla}(\delta h, \hat{\psi})^T \tilde{D}_{N1} \right) \psi_1 + \left(\bar{\nabla}(\delta h, \psi_1) \tilde{D}_{1N}^T + \bar{\nabla}(\delta h, \hat{\psi})^T \tilde{D}_{NN} \right) \hat{\psi} \right) \right. \right. \\ &\quad \left. \left. \left. + H_0 \left(gW \delta h(h - H) - \psi_1 X \tilde{R}_t \delta h_x \right) \right] dx \, dy \right. \right. \\ &\quad \left. \left. + \int_0^{L_y} \left(L_w \tilde{R}_t \left(\psi_1 \tilde{I}_1 + \hat{\psi}^T \tilde{I}_N \right) \delta h \right)_{x=0} dy \right\} dt \implies \right. \\ \int_0^T \int_{\hat{\Omega}_{x,y}} H_0 \partial_t (W\psi_1) \delta h \, dx \, dy \, dt &= - \int_0^T (\delta h; h, \psi_1, \hat{\psi}, R)_{\delta \mathcal{H}_h} + (\delta h; h, \psi_1, \hat{\psi}, R)_{\delta \mathcal{R}_h} \, dt, \end{aligned} \tag{B.1}$$

with $(\delta h; h, \psi_1, \hat{\psi}, R)_{\delta \mathcal{H}_h} \equiv \lim_{\epsilon \rightarrow 0} (\mathcal{H}[h + \epsilon \delta h, \psi_1, \hat{\psi}; R] - \mathcal{H}[h, \psi_1, \hat{\psi}; R]) / \epsilon$, etc., but without performing integrations by parts. Variations of (17) with respect to the surface potential ψ_1 lead to the following weak formulation for the temporal variation of the water depth h :

$$\begin{aligned} \int_0^T \int_{\hat{\Omega}_{x,y}} H_0 \partial_t h \delta(W\psi_1) \, dx \, dy \, dt &= \int_0^T \left\{ \int_{\hat{\Omega}_{x,y}} \left[h \left(\tilde{M}_{11} \bar{\nabla}(\psi_1, \delta\psi_1) + \delta\psi_{1,x} \tilde{M}_{1N}^T \left(\frac{V}{W} \hat{\psi}_x + U \hat{\psi}_y \right) + \delta\psi_{1,y} \tilde{M}_{1N}^T \left(U \hat{\psi}_x + W \hat{\psi}_y \right) \right) \right. \right. \\ &\quad \left. \left. + \frac{\delta\psi_1}{h} \left((\tilde{S}_{11} \psi_1 + \tilde{S}_{1N}^T \hat{\psi}) \bar{\nabla}(h, h) + H_0^2 (\tilde{A}_{11} \psi_1 + \tilde{A}_{1N}^T \hat{\psi}) (\bar{\nabla}(b, b) + W) \right) \right. \right. \\ &\quad \left. \left. + 2H_0 (\tilde{C}_{11} \psi_1 + \tilde{C}_{1N}^T \hat{\psi}) \bar{\nabla}(b, h) \right) \right. \right. \\ &\quad \left. \left. - \left(\left(\bar{\nabla}(h, \psi_1) \tilde{D}_{11} + \bar{\nabla}(h, \hat{\psi})^T \tilde{D}_{N1} \right) \delta\psi_1 + \bar{\nabla}(h, \delta\psi_1) (\tilde{D}_{11} \psi_1 + \tilde{D}_{1N}^T \hat{\psi}) \right) \right. \right. \\ &\quad \left. \left. - H_0 \left(\left(\bar{\nabla}(b, \psi_1) \tilde{B}_{11} + \bar{\nabla}(b, \hat{\psi})^T \tilde{B}_{N1} \right) \delta\psi_1 + \bar{\nabla}(b, \delta\psi_1) (\tilde{B}_{11} \psi_1 + \tilde{B}_{1N}^T \hat{\psi}) \right) \right. \right. \\ &\quad \left. \left. - \delta\psi_1 H_0 X \tilde{R}_t h_x \right] dx \, dy + \int_0^{L_y} \left(L_w \tilde{R}_t \delta\psi_1 \tilde{I}_1 h \right)_{x=0} dy \right\} dt \implies \right. \\ \int_0^T \int_{\hat{\Omega}_{x,y}} H_0 \partial_t h \delta(W\psi_1) \, dx \, dy \, dt &= \int_0^T (\delta\psi_1; h, \psi_1, \hat{\psi}, R)_{\delta \mathcal{H}_{\psi_1}} + (\delta\psi_1; h, \hat{\psi}, R)_{\delta \mathcal{R}_{\psi_1}} \, dt. \end{aligned} \tag{B.2}$$

Finally, variations of (17) with respect to the interior potentials ψ_i lead to linear equations for the interior potentials in terms of the surface potential and water depth:

$$\begin{aligned}
0 = \int_0^T \left\{ \int_{\tilde{\Omega}_{x,y}} \left[h \left(\psi_{1,x} \tilde{M}_{1N}^T \left(\frac{V}{W} \delta \hat{\psi}_x + U \delta \hat{\psi}_y \right) + \psi_{1,y} \tilde{M}_{1N}^T \left(U \delta \hat{\psi}_x + W \delta \hat{\psi}_y \right) \right. \right. \right. \\
+ \frac{V}{W} \hat{\psi}_x^T \tilde{M}_{NN} \delta \hat{\psi}_x + U \left(\delta \hat{\psi}_x^T \tilde{M}_{NN} \hat{\psi}_y + \hat{\psi}_x^T \tilde{M}_{NN} \delta \hat{\psi}_y \right) + W \hat{\psi}_y^T \tilde{M}_{NN} \delta \hat{\psi}_y \\
+ \frac{1}{h} \left(\psi_1 \tilde{S}_{1N}^T \delta \hat{\psi} + \hat{\psi}^T \tilde{S}_{NN} \delta \hat{\psi} \right) \bar{\nabla}(h, h) \\
+ \frac{H_0^2}{h} \left(\psi_1 \tilde{A}_{1N}^T \delta \hat{\psi} + \hat{\psi}^T \tilde{A}_{NN} \delta \hat{\psi} \right) (\bar{\nabla}(b, b) + W) \\
+ \frac{2H_0}{h} \left(\psi_1 \tilde{C}_{1N}^T \delta \hat{\psi} + \hat{\psi}^T \tilde{C}_{NN} \delta \hat{\psi} \right) \bar{\nabla}(b, h) \\
\left. \left. - \left(\bar{\nabla}(h, \delta \hat{\psi})^T \left(\tilde{D}_{N1} \psi_1 + \tilde{D}_{NN} \hat{\psi} \right) + \left(\bar{\nabla}(h, \psi_1) \tilde{D}_{1N}^T + \bar{\nabla}(h, \hat{\psi})^T \tilde{D}_{NN} \right) \delta \hat{\psi} \right) \right. \right. \\
- H_0 \left(\bar{\nabla}(b, \delta \hat{\psi})^T \left(\tilde{B}_{N1} \psi_1 + \tilde{B}_{NN} \hat{\psi} \right) + \left(\bar{\nabla}(b, \psi_1) \tilde{B}_{1N}^T + \bar{\nabla}(b, \hat{\psi})^T \tilde{B}_{NN} \right) \delta \hat{\psi} \right) \left. \right] dx dy \\
\left. \left. + \int_0^{L_y} \left(L_w \tilde{R}_t \delta \hat{\psi}^T \tilde{I}_N h \right)_{x=0} dy \right\} dt \right\} \Rightarrow
\end{aligned} \tag{B.3a}$$

$$\int_0^T (\delta \hat{\psi}; h, \psi_1, \hat{\psi}, R)_{\delta \mathcal{H}_{\hat{\psi}}} dt = - \int_0^T (\delta \hat{\psi}; h, R)_{\delta \mathcal{R}_{\hat{\psi}}} dt \Rightarrow \tag{B.3b}$$

$$\int_0^T (\delta \hat{\psi}, \hat{\psi}; h, R)_{\delta \mathcal{H}_{\hat{\psi},2}} dt = - \int_0^T (\delta \hat{\psi}, \psi_1; h, R)_{\delta \mathcal{H}_{\hat{\psi},1}} + (\delta \hat{\psi}; h, R)_{\delta \mathcal{R}_{\hat{\psi}}} dt. \tag{B.3c}$$

Here we note that the LHS of expression (B.3b) is linear in $\hat{\psi}$ and ψ_1 and the RHS is independent of $\psi_1, \hat{\psi}$, such that we have split up its contributions further in (B.3c).

Appendix C. Symplectic-Euler temporal discretization of weak formulations used in Firedrake

The symplectic-Euler scheme for the abstracted system (22) was given abstractly in the text as (31). In full detail, cf. the implementation in Firedrake, with the test function $\varphi = \delta \psi_1$ below, the first step consists of updating the water depth h , as follows

$$\begin{aligned}
\int_{\tilde{\Omega}_{x,y}} H_0 h^{n+1} W^n \varphi dx dy &= \int_{\tilde{\Omega}_{x,y}} H_0 h^n W^n \varphi dx dy \\
&+ \Delta t \int_{\tilde{\Omega}_{x,y}} \left[h^{n+1} \left(\tilde{M}_{11} \bar{\nabla}^n(\psi_1^n, \varphi) + \varphi_x \tilde{M}_{1N}^T \left(\frac{V^n}{W^n} \hat{\psi}_x^* + U^n \hat{\psi}_y^* \right) + \varphi_y \tilde{M}_{1N}^T \left(U^n \hat{\psi}_x^* + W^n \hat{\psi}_y^* \right) \right) \right. \\
&+ \frac{\varphi}{h^{n+1}} \left(\left(\tilde{S}_{11} \psi_1^n + \tilde{S}_{1N}^T \hat{\psi}^* \right) \bar{\nabla}^n(h^{n+1}, h^{n+1}) + H_0^2 \left(\tilde{A}_{11} \psi_1^n + \tilde{A}_{1N}^T \hat{\psi}^* \right) (\bar{\nabla}^n(b, b) + W^n) \right. \\
&\quad \left. \left. + 2H_0 \left(\tilde{C}_{11} \psi_1^n + \tilde{C}_{1N}^T \hat{\psi}^* \right) \bar{\nabla}^n(b, h^{n+1}) \right) \right. \\
&- \left(\left(\bar{\nabla}^n(h^{n+1}, \psi_1^n) \tilde{D}_{11} + \bar{\nabla}^n(h^{n+1}, \hat{\psi}^*)^T \tilde{D}_{N1} \right) \varphi + \bar{\nabla}^n(h^{n+1}, \varphi) (\tilde{D}_{11} \psi_1^n + \tilde{D}_{1N}^T \hat{\psi}^*) \right) \\
&- H_0 \left(\left(\bar{\nabla}^n(b, \psi_1^n) \tilde{B}_{11} + \bar{\nabla}^n(b, \hat{\psi}^*)^T \tilde{B}_{N1} \right) \varphi + \bar{\nabla}^n(b, \varphi) (\tilde{B}_{11} \psi_1^n + \tilde{B}_{1N}^T \hat{\psi}^*) \right) \\
&\quad \left. - \varphi H_0 X \tilde{R}_t^n h_x^{n+1} \right] dx dy + \Delta t \int_0^{L_y} \left(L_w \tilde{R}_t^n \varphi \tilde{I}_1 h^{n+1} \right)_{x=0} dy
\end{aligned} \tag{C.1}$$

and simultaneously for the interior potential $\hat{\psi}^*$, with now $\hat{\phi} = \delta\hat{\psi}$, by solving

$$\begin{aligned}
0 = \int_{\hat{\Omega}_{x,y}} & \left[h^{n+1} \left(\psi_{1,x}^n \tilde{M}_{1N}^T \left(\frac{V^n}{W^n} \hat{\phi}_x + U^n \hat{\phi}_y \right) + \psi_{1,y}^n \tilde{M}_{1N}^T \left(U^n \hat{\phi}_x + W^n \hat{\phi}_y \right) \right. \right. \\
& + \frac{V^n}{W^n} \hat{\psi}_x^{*T} \tilde{M}_{NN} \hat{\phi}_x + U^n \left(\hat{\phi}_x^T \tilde{M}_{NN} \hat{\psi}_y^* + \hat{\psi}_x^{*T} \tilde{M}_{NN} \hat{\phi}_y \right) + W^n \hat{\psi}_y^{*T} \tilde{M}_{NN} \hat{\phi}_y \Big) \\
& + \frac{1}{h^{n+1}} \left(\psi_1^n \tilde{S}_{1N}^T \hat{\phi} + \hat{\psi}^{*T} \tilde{S}_{NN} \hat{\phi} \right) \bar{\nabla}^n(h^{n+1}, h^{n+1}) + \frac{H_0^2}{h^{n+1}} \left(\psi_1^n \tilde{A}_{1N}^T \hat{\phi} + \hat{\psi}^{*T} \tilde{A}_{NN} \hat{\phi} \right) (\bar{\nabla}^n(b, b) + W^n) \\
& \left. \left. + \underbrace{\frac{2H_0}{h^{n+1}} \left(\psi_1^n \tilde{C}_{1N}^T \hat{\phi} + \hat{\psi}^{*T} \tilde{C}_{NN} \hat{\phi} \right) \bar{\nabla}^n(b, h^{n+1})}_{-} \right) \right] \\
& - \left(\bar{\nabla}^n(h^{n+1}, \hat{\phi})^T \left(\tilde{D}_{N1} \psi_1^n + \tilde{D}_{NN} \hat{\psi}^* \right) + \left(\bar{\nabla}^n(h^{n+1}, \psi_1^n) \tilde{D}_{1N}^T + \bar{\nabla}^n(h^{n+1}, \hat{\psi}^*)^T \tilde{D}_{NN} \right) \hat{\phi} \right) \\
& - H_0 \left(\bar{\nabla}^n(b, \hat{\phi})^T \left(\tilde{B}_{N1} \psi_1^n + \tilde{B}_{NN} \hat{\psi}^* \right) + \left(\bar{\nabla}^n(b, \psi_1^n) \tilde{B}_{1N}^T + \bar{\nabla}^n(b, \hat{\psi}^*)^T \tilde{B}_{NN} \right) \hat{\phi} \right) \Big] dx dy \\
& + \int_0^{L_y} \left(L_w \tilde{R}_t^n \hat{\phi}^T \tilde{I}_N h^{n+1} \right)_{x=0} dy.
\end{aligned} \tag{C.2}$$

Equation (C.2) is a system of n_z equations, concerning the DtN-operator, each one eliminating the velocity potential in one of the vertical subsurface layers. The second and final step is then to update the surface velocity potential ψ_1 with $\varphi = \delta h$ and the following pseudo-semi-implicit equation (C.3), the terminology reflecting the observation that in this case h^{n+1} has already been calculated using (C.1):

$$\begin{aligned}
\int_{\hat{\Omega}_{x,y}} H_0 \left(W^{n+1} \psi_1^{n+1} \right) \varphi dx dy &= \int_{\hat{\Omega}_{x,y}} H_0 \left(W^n \psi_1^n \right) \varphi dx dy \\
&- \Delta t \int_{\hat{\Omega}_{x,y}} \left[\frac{\varphi}{2} \left(\tilde{M}_{11} \bar{\nabla}^n(\psi_1^n, \psi_1^n) + 2\psi_{1,x}^n \tilde{M}_{1N}^T \left(\frac{V^n}{W^n} \hat{\psi}_x^* + U^n \hat{\psi}_y^* \right) \right. \right. \\
&+ 2\psi_{1,y}^n \tilde{M}_{1N}^T \left(U^n \hat{\psi}_x^* + W^n \hat{\psi}_y^* \right) + \frac{V^n}{W^n} \hat{\psi}_x^{*T} \tilde{M}_{NN} \hat{\psi}_x^* + 2U^n \hat{\psi}_x^{*T} \tilde{M}_{NN} \hat{\psi}_y^* + W^n \hat{\psi}_y^{*T} \tilde{M}_{NN} \hat{\psi}_y^* \\
&+ \frac{1}{h^{n+1}} \left(\psi_1^n \tilde{S}_{11} \psi_1^n + 2\psi_1^n \tilde{S}_{1N}^T \hat{\psi}^* + \hat{\psi}^{*T} \tilde{S}_{NN} \hat{\psi}^* \right) \left(\bar{\nabla}^n(h^{n+1}, \varphi) - \frac{\varphi}{2h^{n+1}} \bar{\nabla}^n(h^{n+1}, h^{n+1}) \right) \\
&- \frac{H_0^2}{2h^{n+1}^2} \varphi \left(\psi_1^n \tilde{A}_{11} \psi_1^n + 2\psi_1^n \tilde{A}_{1N}^T \hat{\psi}^* + \hat{\psi}^{*T} \tilde{A}_{NN} \hat{\psi}^* \right) (\bar{\nabla}^n(b, b) + W^n) \\
&+ \underbrace{\frac{H_0}{h^{n+1}} \left(\psi_1^n \tilde{C}_{11} \psi_1^n + 2\psi_1^n \tilde{C}_{1N}^T \hat{\psi}^* + \hat{\psi}^{*T} \tilde{C}_{NN} \hat{\psi}^* \right)}_{-} \left(\bar{\nabla}^n(b, \varphi) - \frac{\varphi}{h^{n+1}} \bar{\nabla}^n(b, h^{n+1}) \right) \\
&- \left(\left(\bar{\nabla}^n(\varphi, \psi_1^n) \tilde{D}_{11} + \bar{\nabla}^n(\varphi, \hat{\psi}^*)^T \tilde{D}_{N1} \right) \psi_1^n + \left(\bar{\nabla}^n(\varphi, \psi_1^n) \tilde{D}_{1N}^T + \bar{\nabla}^n(\varphi, \hat{\psi}^*)^T \tilde{D}_{NN} \right) \hat{\psi}^* \right) \\
&+ H_0 \left(g W^n \varphi (h^{n+1} - H) - \psi_1^n X \tilde{R}_t^n \varphi_x \right) \Big] dx dy - \Delta t \int_0^{L_y} \left(L_w \tilde{R}_t^n \left(\psi_1^n \tilde{I}_1 + \hat{\psi}^{*T} \tilde{I}_N \right) \varphi \right)_{x=0} dy.
\end{aligned} \tag{C.3}$$

Note that in the above weak formulations (C.1)–(C.3), the wavy-underlined terms will be neglected in the computational model if the MSA is applied.

Appendix D. Störmer-Verlet temporal discretization of weak formulations used in Firedrake

The Störmer-Verlet scheme for the abstracted system (22) was given in the main text as (32). In full detail, cf. the implementation in Firedrake, the first step consists of updating the surface velocity potential at intermediate time

$t^{n+1/2}$, as follows

$$\begin{aligned}
\int_{\tilde{\Omega}_{x,y}} H_0 \left(W^{n+1/2} \psi_1^{n+1/2} \right) \varphi \, dx \, dy &= \int_{\tilde{\Omega}_{x,y}} H_0 \left(W^n \psi_1^n \right) \varphi \, dx \, dy \\
&\quad - \frac{\Delta t}{2} \int_{\tilde{\Omega}_{x,y}} \left[\frac{\varphi}{2} \left(\tilde{M}_{11} \bar{\nabla}^{n+1/2} (\psi_1^{n+1/2}, \psi_1^{n+1/2}) + 2\psi_{1,x}^{n+1/2} \tilde{M}_{1N}^T \left(\frac{V^{n+1/2}}{W^{n+1/2}} \hat{\psi}_x^* + U^{n+1/2} \hat{\psi}_y^* \right) \right. \right. \\
&\quad \left. \left. + 2\psi_{1,y}^{n+1/2} \tilde{M}_{1N}^T \left(U^{n+1/2} \hat{\psi}_x^* + W^{n+1/2} \hat{\psi}_y^* \right) + \frac{V^{n+1/2}}{W^{n+1/2}} \hat{\psi}_x^{*T} \tilde{M}_{NN} \hat{\psi}_x^* + 2U^{n+1/2} \hat{\psi}_x^{*T} \tilde{M}_{NN} \hat{\psi}_y^* + W^{n+1/2} \hat{\psi}_y^{*T} \tilde{M}_{NN} \hat{\psi}_y^* \right) \right. \\
&\quad \left. + \frac{1}{h^n} \left(\psi_1^{n+1/2} \tilde{S}_{11} \psi_1^{n+1/2} + 2\psi_1^{n+1/2} \tilde{S}_{1N}^T \hat{\psi}_N^* + \hat{\psi}_N^{*T} \tilde{S}_{NN} \hat{\psi}_N^* \right) \left(\bar{\nabla}^{n+1/2} (h^n, \varphi) - \frac{\varphi}{2h^n} \bar{\nabla}^{n+1/2} (h^n, h^n) \right) \right. \\
&\quad \left. - \frac{H_0^2}{2h^{n/2}} \varphi \left(\psi_1^{n+1/2} \tilde{A}_{11} \psi_1^{n+1/2} + 2\psi_1^{n+1/2} \tilde{A}_{1N}^T \hat{\psi}_N^* + \hat{\psi}_N^{*T} \tilde{A}_{NN} \hat{\psi}_N^* \right) \left(\bar{\nabla}^{n+1/2} (b, b) + W^{n+1/2} \right) \right. \\
&\quad \left. + \frac{H_0}{h^n} \left(\psi_1^{n+1/2} \tilde{C}_{11} \psi_1^{n+1/2} + 2\psi_1^{n+1/2} \tilde{C}_{1N}^T \hat{\psi}_N^* + \hat{\psi}_N^{*T} \tilde{C}_{NN} \hat{\psi}_N^* \right) \left(\bar{\nabla}^{n+1/2} (b, \varphi) - \frac{\varphi}{h^n} \bar{\nabla}^{n+1/2} (b, h^n) \right) \right. \\
&\quad \left. - \left(\left(\bar{\nabla}^{n+1/2} (\varphi, \psi_1^{n+1/2}) \tilde{D}_{11} + \bar{\nabla}^{n+1/2} (\varphi, \hat{\psi}^*)^T \tilde{D}_{N1} \right) \psi_1^{n+1/2} + \left(\bar{\nabla}^{n+1/2} (\varphi, \psi_1^{n+1/2}) \tilde{D}_{1N}^T + \bar{\nabla}^{n+1/2} (\varphi, \hat{\psi}^*)^T \tilde{D}_{NN} \right) \hat{\psi}^* \right) \right. \\
&\quad \left. + H_0 \left(g W^{n+1/2} \varphi (h^n - H) - \psi_1^{n+1/2} X \tilde{R}_t^{n+1/2} \varphi_x \right) \right] dx \, dy - \frac{\Delta t}{2} \int_0^{L_y} \left(L_w \tilde{R}_t^{n+1/2} \left(\psi_1^{n+1/2} \tilde{I}_1 + \hat{\psi}_N^{*T} \tilde{I}_N \right) \varphi \right)_{x=0} dy
\end{aligned} \tag{D.1}$$

simultaneously solving for the interior potential $\hat{\psi}^*$ with test vector $\hat{\varphi} = \delta \hat{\psi}$ as follows

$$\begin{aligned}
0 = \int_{\tilde{\Omega}_{x,y}} & \left[h^n \left(\psi_{1,x}^{n+1/2} \tilde{M}_{1N}^T \left(\frac{V^{n+1/2}}{W^{n+1/2}} \hat{\varphi}_x + U^{n+1/2} \hat{\varphi}_y \right) + \psi_{1,y}^{n+1/2} \tilde{M}_{1N}^T \left(U^{n+1/2} \hat{\varphi}_x + W^{n+1/2} \hat{\varphi}_y \right) \right. \right. \\
& \left. + \frac{V^{n+1/2}}{W^{n+1/2}} \hat{\psi}_x^{*T} \tilde{M}_{NN} \hat{\varphi}_x + U^{n+1/2} \left(\hat{\varphi}_x^T \tilde{M}_{NN} \hat{\psi}_y^* + \hat{\psi}_x^{*T} \tilde{M}_{NN} \hat{\varphi}_y \right) + W^{n+1/2} \hat{\psi}_y^{*T} \tilde{M}_{NN} \hat{\varphi}_y \right) \\
& \left. + \frac{1}{h^n} \left(\psi_1^{n+1/2} \tilde{S}_{1N}^T \hat{\varphi} + \hat{\psi}_N^{*T} \tilde{S}_{NN} \hat{\varphi} \right) \bar{\nabla}^{n+1/2} (h^n, h^n) + \frac{H_0^2}{h^n} \left(\psi_1^{n+1/2} \tilde{A}_{1N}^T \hat{\varphi} + \hat{\psi}_N^{*T} \tilde{A}_{NN} \hat{\varphi} \right) \left(\bar{\nabla}^{n+1/2} (b, b) + W^{n+1/2} \right) \right. \\
& \left. + \frac{2H_0}{h^n} \left(\psi_1^{n+1/2} \tilde{C}_{1N}^T \hat{\varphi} + \hat{\psi}_N^{*T} \tilde{C}_{NN} \hat{\varphi} \right) \bar{\nabla}^{n+1/2} (b, h^n) \right. \\
& \left. - \left(\bar{\nabla}^{n+1/2} (h^n, \hat{\varphi})^T \left(\tilde{D}_{N1} \psi_1^{n+1/2} + \tilde{D}_{NN} \hat{\psi}^* \right) + \left(\bar{\nabla}^{n+1/2} (h^n, \psi_1^{n+1/2}) \tilde{D}_{1N}^T + \bar{\nabla}^{n+1/2} (h^n, \hat{\psi}^*)^T \tilde{D}_{NN} \right) \hat{\varphi} \right) \right. \\
& \left. - H_0 \left(\bar{\nabla}^{n+1/2} (b, \hat{\varphi})^T \left(\tilde{B}_{N1} \psi_1^{n+1/2} + \tilde{B}_{NN} \hat{\psi}^* \right) + \left(\bar{\nabla}^{n+1/2} (b, \psi_1^{n+1/2}) \tilde{B}_{1N}^T + \bar{\nabla}^{n+1/2} (b, \hat{\psi}^*)^T \tilde{B}_{NN} \right) \hat{\varphi} \right) \right] dx \, dy \\
& + \int_0^{L_y} \left(L_w \tilde{R}_t^{n+1/2} \hat{\varphi}^T \tilde{I}_N h^n \right)_{x=0} dy.
\end{aligned} \tag{D.2}$$

Equation (D.2) is actually a system of n_z equations, each one eliminating the velocity potential in one of the vertical subsurface layers. The second step is then to update the depth h with the following semi-implicit equation:

$$\begin{aligned}
& \int_{\hat{\Omega}_{x,y}} \varphi H_0 W^{n+1/2} h^{n+1} dx dy = \int_{\hat{\Omega}_{x,y}} \varphi H_0 W^{n+1/2} h^n dx dy \\
& + \frac{\Delta t}{2} \left\{ \int_{\hat{\Omega}_{x,y}} \left[\frac{\varphi}{h^n} \left((\tilde{S}_{11} \psi_1^{n+1/2} + \tilde{S}_{1N}^T \hat{\psi}^*) \bar{\nabla}^{n+1/2} (h^n, h^n) + H_0^2 (\tilde{A}_{11} \psi_1^{n+1/2} + \tilde{A}_{1N}^T \hat{\psi}^*) (\bar{\nabla}^{n+1/2} (b, b) + W^{n+1/2}) \right. \right. \right. \\
& \quad \left. \left. \left. + 2H_0 (\tilde{C}_{11} \psi_1^{n+1/2} + \tilde{C}_{1N}^T \hat{\psi}^*) \bar{\nabla}^{n+1/2} (b, h^n) \right] + h^n \left[\bar{\nabla}^{n+1/2} (\psi_1^{n+1/2}, \varphi) \tilde{M}_{11} + \bar{\nabla}^{n+1/2} (\hat{\psi}^*, \varphi)^T \tilde{M}_{N1} \right] \right. \right. \\
& \quad \left. \left. - \left[(\tilde{D}_{11} \psi_1^{n+1/2} + \tilde{D}_{1N}^T \hat{\psi}^*) \bar{\nabla}^{n+1/2} (h^n, \varphi) + (\tilde{D}_{11} \bar{\nabla}^{n+1/2} (h^n, \psi_1^{n+1/2}) + \bar{\nabla}^{n+1/2} (h^n, \hat{\psi}^*)^T \tilde{D}_{N1}) \varphi \right] \right. \right. \\
& \quad \left. \left. - H_0 \left[(\tilde{B}_{11} \psi_1^{n+1/2} + \tilde{B}_{1N}^T \hat{\psi}^*) \bar{\nabla}^{n+1/2} (b, \varphi) + (\bar{\nabla}^{n+1/2} (b, \psi_1^{n+1/2}) \tilde{B}_{11} + \bar{\nabla}^{n+1/2} (b, \hat{\psi}^*)^T \tilde{B}_{N1}) \varphi \right] \right. \right. \\
& \quad \left. \left. - (\varphi H_0 X \tilde{R}_t^{n+1/2} h_x^n) \right] dx dy + \int_0^{L_y} (L_w \tilde{R}_t^{n+1/2} \varphi \tilde{I}_1 h^n)_{x=0} dy \right\} \\
& + \int_{\hat{\Omega}_{x,y}} \left[\frac{\varphi}{h^{n+1}} \left((\tilde{S}_{11} \psi_1^{n+1/2} + \tilde{S}_{1N}^T \hat{\psi}^\ddagger) \bar{\nabla}^{n+1/2} (h^{n+1}, h^{n+1}) + H_0^2 (\tilde{A}_{11} \psi_1^{n+1/2} + \tilde{A}_{1N}^T \hat{\psi}^\ddagger) (\bar{\nabla}^{n+1/2} (b, b) + W^{n+1/2}) \right. \right. \\
& \quad \left. \left. + 2H_0 (\tilde{C}_{11} \psi_1^{n+1/2} + \tilde{C}_{1N}^T \hat{\psi}^\ddagger) \bar{\nabla}^{n+1/2} (b, h^{n+1}) \right] + h^{n+1} \left[\bar{\nabla}^{n+1/2} (\psi_1^{n+1/2}, \varphi) \tilde{M}_{11} + \bar{\nabla}^{n+1/2} (\hat{\psi}^\ddagger, \varphi)^T \tilde{M}_{N1} \right] \right. \right. \\
& \quad \left. \left. - \left[(\tilde{D}_{11} \psi_1^{n+1/2} + \tilde{D}_{1N}^T \hat{\psi}^\ddagger) \bar{\nabla}^{n+1/2} (h^{n+1}, \varphi) + (\tilde{D}_{11} \bar{\nabla}^{n+1/2} (h^{n+1}, \psi_1^{n+1/2}) + \bar{\nabla}^{n+1/2} (h^{n+1}, \hat{\psi}^\ddagger)^T \tilde{D}_{N1}) \varphi \right] \right. \right. \\
& \quad \left. \left. - H_0 \left[(\tilde{B}_{11} \psi_1^{n+1/2} + \tilde{B}_{1N}^T \hat{\psi}^\ddagger) \bar{\nabla}^{n+1/2} (b, \varphi) + (\bar{\nabla}^{n+1/2} (b, \psi_1^{n+1/2}) \tilde{B}_{11} + \bar{\nabla}^{n+1/2} (b, \hat{\psi}^\ddagger)^T \tilde{B}_{N1}) \varphi \right] \right. \right. \\
& \quad \left. \left. - (\varphi H_0 X \tilde{R}_t^{n+1/2} h_x^{n+1}) \right] dx dy + \int_0^{L_y} (L_w \tilde{R}_t^{n+1/2} \varphi \tilde{I}_1 h^{n+1})_{x=0} dy \right\},
\end{aligned} \tag{D.3}$$

simultaneously with

$$\begin{aligned}
0 = & \int_{\hat{\Omega}_{x,y}} \left[h^{n+1} \left(\psi_{1,x}^{n+1/2} \tilde{M}_{1N}^T \left(\frac{V^{n+1/2}}{W^{n+1/2}} \hat{\phi}_x + U^{n+1/2} \hat{\phi}_y \right) + \psi_{1,y}^{n+1/2} \tilde{M}_{1N}^T \left(U^{n+1/2} \hat{\phi}_x + W^{n+1/2} \hat{\phi}_y \right) \right. \right. \\
& + \frac{V^{n+1/2}}{W^{n+1/2}} \hat{\psi}_x^{\ddagger T} \tilde{M}_{NN} \hat{\phi}_x + U^{n+1/2} \left(\hat{\phi}_x^T \tilde{M}_{NN} \hat{\psi}_y^\ddagger + \hat{\psi}_x^{\ddagger T} \tilde{M}_{NN} \hat{\phi}_y \right) + W^{n+1/2} \hat{\psi}_y^{\ddagger T} \tilde{M}_{NN} \hat{\phi}_y \Big) \\
& + \frac{1}{h^{n+1}} \left(\psi_1^{n+1/2} \tilde{S}_{1N}^T \hat{\phi} + \hat{\psi}^{\ddagger T} \tilde{S}_{NN} \hat{\phi} \right) \bar{\nabla}^{n+1/2} (h^{n+1}, h^{n+1}) + \frac{H_0^2}{h^{n+1}} \left(\psi_1^{n+1/2} \tilde{A}_{1N}^T \hat{\phi} + \hat{\psi}^{\ddagger T} \tilde{A}_{NN} \hat{\phi} \right) (\bar{\nabla}^{n+1/2} (b, b) + W^{n+1/2}) \\
& + \frac{2H_0}{h^{n+1}} \left(\psi_1^{n+1/2} \tilde{C}_{1N}^T \hat{\phi} + \hat{\psi}^{\ddagger T} \tilde{C}_{NN} \hat{\phi} \right) \bar{\nabla}^{n+1/2} (b, h^{n+1}) \\
& - \left(\bar{\nabla}^{n+1/2} (h^{n+1}, \hat{\phi})^T \left(\tilde{D}_{N1} \psi_1^{n+1/2} + \tilde{D}_{NN} \hat{\psi}^\ddagger \right) + \left(\bar{\nabla}^{n+1/2} (h^{n+1}, \psi_1^{n+1/2}) \tilde{D}_{1N}^T + \bar{\nabla}^{n+1/2} (h^{n+1}, \hat{\psi}^\ddagger)^T \tilde{D}_{NN} \right) \hat{\phi} \right) \\
& - H_0 \left(\bar{\nabla}^{n+1/2} (b, \hat{\phi})^T \left(\tilde{B}_{N1} \psi_1^{n+1/2} + \tilde{B}_{NN} \hat{\psi}^\ddagger \right) + \left(\bar{\nabla}^{n+1/2} (b, \psi_1^{n+1/2}) \tilde{B}_{1N}^T + \bar{\nabla}^{n+1/2} (b, \hat{\psi}^\ddagger)^T \tilde{B}_{NN} \right) \hat{\phi} \right) \Big] dx dy \\
& + \int_0^{L_y} (L_w \tilde{R}_t^{n+1/2} \hat{\phi}^T \tilde{I}_N h^{n+1})_{x=0} dy.
\end{aligned} \tag{D.4}$$

Finally, the surface potential with $\delta h = \varphi$ is updated by solving

$$\begin{aligned}
\int_{\hat{\Omega}_{x,y}} \varphi H_0(W^{n+1} \psi_1^{n+1}) dx dy &= \int_{\hat{\Omega}_{x,y}} \varphi H_0(W^{n+1/2} \psi_1^{n+1/2}) dx dy \\
&\quad - \frac{\Delta t}{2} \left\{ \int_{\hat{\Omega}_{x,y}} \left[-\frac{H_0^2}{2(h^{n+1})^2} \varphi (\psi_1^{n+1/2} \tilde{A}_{11} \psi_1^{n+1/2} + \hat{\psi}^{\ddagger T} \tilde{A}_{NN} \hat{\psi}^{\ddagger} + 2\psi_1^{n+1/2} \tilde{A}_{1N}^T \hat{\psi}^{\ddagger}) (\overline{\nabla}^{n+1/2}(b, b) + W^{n+1/2}) \right. \right. \\
&\quad + \frac{1}{h^{n+1}} \left(-\frac{\varphi}{2h^{n+1}} \overline{\nabla}^{n+1/2}(h^{n+1}, h^{n+1}) + \overline{\nabla}^{n+1/2}(h^{n+1}, \varphi) \right) (\psi_1^{n+1/2} \tilde{S}_{11} \psi_1^{n+1/2} + \hat{\psi}^{\ddagger T} \tilde{S}_{NN} \hat{\psi}^{\ddagger} + 2\psi_1^{n+1/2} \tilde{S}_{1N}^T \hat{\psi}^{\ddagger}) \\
&\quad + \underbrace{\frac{H_0}{h^{n+1}} \left(-\frac{\varphi}{h^{n+1}} \overline{\nabla}^{n+1/2}(b, h^{n+1}) + \overline{\nabla}^{n+1/2}(b, \varphi) \right) (\psi_1^{n+1/2} \tilde{C}_{11} \psi_1^{n+1/2} + \hat{\psi}^{\ddagger T} \tilde{C}_{NN} \hat{\psi}^{\ddagger} + 2\psi_1^{n+1/2} \tilde{C}_{1N}^T \hat{\psi}^{\ddagger})}_{-\overline{\nabla}^{n+1/2}(\varphi, \psi_1^{n+1/2}) (\tilde{D}_{11} \psi_1^{n+1/2} + \tilde{D}_{1N}^T \hat{\psi}^{\ddagger}) - \overline{\nabla}^{n+1/2}(\varphi, \hat{\psi}^{\ddagger})^T (\tilde{D}_{N1} \psi_1^{n+1/2} + \tilde{D}_{NN} \hat{\psi}^{\ddagger})} \\
&\quad + \frac{\varphi}{2} \left(\tilde{M}_{11} \overline{\nabla}^{n+1/2}(\psi_1^{n+1/2}, \psi_1^{n+1/2}) + 2\overline{\nabla}^{n+1/2}(\psi_1^{n+1/2}, \hat{\psi}^{\ddagger})^T \tilde{M}_{N1} \right) \\
&\quad + \frac{\varphi}{2} \left(\frac{V^{n+1/2}}{W^{n+1/2}} \hat{\psi}_x^{\ddagger T} \tilde{M}_{NN} \hat{\psi}_x^{\ddagger} + W^{n+1/2} \hat{\psi}_y^{\ddagger T} \tilde{M}_{NN} \hat{\psi}_y^{\ddagger} + 2U^{n+1/2} \hat{\psi}_x^{\ddagger T} \tilde{M}_{NN} \hat{\psi}_y^{\ddagger} \right) \\
&\quad + H_0 \left(g W^{n+1/2} \varphi (h^{n+1} - H) - \psi_1^{n+1/2} X \tilde{R}_t^{n+1/2} \varphi_x \right) \Big| dx dy \\
&\quad + \int_0^{L_y} \left(L_w \tilde{R}_t^{n+1/2} (\psi_1^{n+1/2} \tilde{I}_1 + \hat{\psi}^{\ddagger T} \tilde{I}_N) \varphi \right)_{x=0} dy \Big\},
\end{aligned} \tag{D.5}$$

which is an explicit step for ψ_1^{n+1} . Note that in the above weak formulations (D.1)–(D.5), the wavy-underlined terms will be neglected in the computational model if the MSA is applied.

References

- [1] M. Onorato, A. Osborne, M. Serio, L. Cavaleri, C. Brandini, C. Stansberg, Extreme waves, modulational instability and second order theory: wave flume experiments on irregular waves, European J. of Mech. - B/Fluids 25 (2006) 586–601. Rogue waves European Geosciences Union Assembly.
- [2] J. Hennig, C. E. Schmittner, Experimental variation of focusing wave groups for the investigation of their predictability, in: Proc. ASME 2009 28th Int. Conf. Offshore Mechanics and Arctic Engineering, Volume 6, Honolulu, Hawaii, USA, 2009, pp. 641–651.
- [3] J. Chambarel, C. Kharif, O. Kimmoun, Generation of two-dimensional steep water waves on finite depth with and without wind, European J. of Mech. -B/Fluids 29 (2010) 132–142.
- [4] D. Peregrine, Water waves, nonlinear Schrödinger equations and their solutions, J. Austral. Math. Soc. Ser. B 25 (1983) 16–43.
- [5] A. Chabchoub, N. Hoffmann, N. Akhmediev, Rogue wave observation in a water wave tank, Phys. Rev. Letters 106 (2011).
- [6] G. F. Clauss, C. E. Schmittner, J. Hennig, C. Guedes Soares, N. Fonseca, R. Pascoal, Bending moments of an fpo in rogue waves, in: Proc. ASME 2004 23rd International Conference on Offshore Mechanics and Arctic Engineering, Volume 2, Vancouver, British Columbia, Canada, 2004, pp. 455–462.
- [7] E. Bitner-Gregersen, O. Gramstad, Rogue waves. impact on ships and offshore structures, DNV GL strategic research and innovation Position paper (2016).
- [8] E. Gagarina, A. Ambati, J. van der Vegt, O. Bokhove, Variational space-time (dis)continuous Galerkin method for nonlinear free surface water waves, J. Com. Phys. 275 (2014) 459–483.
- [9] Q. Ma, G. Wu, R. E. Taylor, Finite element simulation of fully nonlinear interaction between vertical cylinders and steep waves. Part 1: Numerical results and validation, Int. J. Numer. Methods Fluids 36 (2001) 265–285.
- [10] Q. Ma, G. Wu, R. E. Taylor, Finite element simulation of fully nonlinear interaction between vertical cylinders and steep waves. Part 2: Methodology and numerical procedure, Int. J. Numer. Methods Fluids 36 (2001) 287–308.
- [11] Q. Ma, S. Yan, Quasi ALE finite element method for nonlinear water waves, J. Comp. Phys. 212 (2006) 52–72.
- [12] G. Wu, Z. Hu, Simulation of nonlinear interactions between waves and floating bodies through a finite-element-based numerical tank, Proc. Roy. Soc. Lond. Ser. A 460 (2004) 2797–2817.
- [13] A. Engsig-Karup, H. Bingham, O. Lindberg, An efficient flexible-order model for 3D nonlinear water waves, J. Comp. Phys. 228 (2009) 2100–2118.
- [14] J. Luke, A variational principle for a fluid with a free surface, J. Fluid Mech. 27 (1967) 395–397.
- [15] J. Kim, K. Bai, A finite element method for two-dimensional water-wave problems, Numerical Methods in Fluids 30 (1999) 105–122.
- [16] E. Gagarina, V. Ambati, S. Nurjanyan, J. van der Vegt, O. Bokhove, On variational and symplectic time integrators for Hamiltonian systems, J. Comp. Phys. 306 (2016) 370–389.
- [17] F. Rathgeber, D. A. Ham, L. Mitchell, M. Lange, F. Luporini, A. T. T. Mcrae, G. Bercea, G. R. Markall, P. H. J. Kelly, Firedrake: Automating the finite element method by composing abstractions, ACM Trans. Math. Softw. 43 (2016).

- [18] S. Balay, W. D. Gropp, L. C. McInnes, B. F. Smith, Efficient management of parallelism in object oriented numerical software libraries, in: E. Arge, A. M. Bruaset, H. P. Langtangen (Eds.), *Modern Software Tools in Scientific Computing*, Birkhäuser Press, 1997, pp. 163–202.
- [19] S. Balay, S. Abhyankar, M. F. Adams, J. Brown, P. Brune, K. Buschelman, L. Dalcin, V. Eijkhout, W. D. Gropp, D. Kaushik, M. G. Knepley, L. C. McInnes, K. Rupp, B. F. Smith, S. Zampini, H. Zhang, H. Zhang, PETSc Users Manual, Technical Report ANL-95/11 - Revision 3.7, Argonne National Laboratory, 2016. URL: <http://www.mcs.anl.gov/petsc>.
- [20] M. Homolya, D. Ham, A parallel edge orientation algorithm for quadrilateral meshes., *SIAM Journal on Scientific Computing* 38 (2016) S48–S61.
- [21] A. MacRae, G. Bercea, L. Mitchell, D. Ham, C. J. Cotter, Automated generation and symbolic manipulation of tensor product finite elements, *SIAM J. Sci. Comp.* 38 (2016) 25–S47.
- [22] T. Bunnik, Benchmark workshop on numerical wave modelling—description of test cases, Technical Report 70022-1-RD, MARIN, 2010.
- [23] J. W. Miles, Obliquely interacting solitary waves, *J. Fluid Mech.* 79 (1977) 157–169.
- [24] J. N. Reddy, *An introduction to the Finite Element Method*, McGraw-Hill, 2005.
- [25] W. Craig, C. Sulem, Numerical simulation of gravity waves, *J. Comp. Phys.* 108 (1992) 73–83.
- [26] O. Bokhove, A. Kalogirou, Variational water wave modelling: from continuum to experiment, in: T. Bridges, M. Groves, D. Nicholls (Eds.), *Lectures on the theory of water waves*, volume 426 of *LMS Lecture Note Series*, Cambridge University Press, 2016, pp. 226–260.
- [27] E. Hairer, C. Lubich, G. Wanner, *Geometric Numerical Integration*, Springer, 2006.
- [28] E. Hairer, C. Lubich, G. Wanner, Geometric numerical integration illustrated by the Störmer-Verlet method, *Acta Numerica* 12 (2003) 399–450.
- [29] F. Gidel, Variational water-wave models and pyramidal freak waves, Ph.D. thesis, University of Leeds, 2018. URL: <http://etheses.whiterose.ac.uk/21730/>.
- [30] G. D. Smith, *Numerical Solution of Partial Differential Equations: Finite-difference methods*, 2nd. ed., Clarendon Press, Oxford, 1978, p. 217.
- [31] A. Kalogirou, E. E. Moulopoulou, O. Bokhove, Variational finite element methods for waves in a Hele-Shaw tank, *Applied Mathematical Modelling* 40 (2016) 7493–7503.
- [32] F. Gidel, O. Bokhove, A. Kalogirou, Variational modelling of extreme waves through oblique interaction of solitary waves: application to mach reflection, *Nonlinear Proc. Geophys.* 24 (2017) 43–60.
- [33] C. Baker, *Making a splash with solitons*, Master's thesis, University of Leeds, School of Mathematics, 2017.
- [34] J. Choi, O. Bokhove, A. Kalogirou, M. A. Kelmans, Numerical experiments on extreme waves through oblique-soliton interactions, *Water Waves*, in press (2022).
- [35] W. Wang, C. Pakozdi, A. Kamath, H. Bihs, A fully nonlinear potential flow wave modelling procedure for simulations of offshore sea states with various wave breaking scenarios, *Applied Ocean Res.* 117 (2021) 102898.
- [36] S. Ritchie, *Science fictions: Exposing fraud, bias, negligence and hype in science*, Vintage UK, 2021.

Appendix E. Supplementary material: details of simulations

In addition to the code descriptions in the GitHub organization, we provide below in Table E.3 a brief overview of the simulations of the test cases TC1–TC4.

Simulation	Solver	$T_{end}, \Delta t, \Delta t_{save}$ $\Delta x, \Delta y, N_z$	Table	Settings & cores used
Sect. 4.1/TC1	SE/SV 2D	$T_{end} = 4.3\text{s}, \Delta t = (0.0159, 0.0079)\text{s}, \Delta t_{save} = \Delta t$ $\Delta x = 0.05\text{m}, N_z = 7$	-	no wavemaker, flat bottom $H_0 = 1.136\text{m}, L_x = 6.283\text{m}$ two time resolutions, one core
Sect. 4.2.1/TC2	SE/SV 3D	$T_{end} = 7\text{s}, \Delta t = 0.002\text{s}, \Delta t_{save} = \Delta t$ $\Delta x = \Delta y = (0.1, 0.05, 0.025)\text{m}, N_z = 9$	1	mild-slope approximation three spatial resolutions 8 cores
Sect. 4.2.2/TC2b	SE/SV 3D	$T_{end} = 7\text{s}, \Delta t = 0.002\text{s}, \Delta t_{save} = \Delta t$ $\Delta x = \Delta y = (0.1, 0.05, 0.025)\text{m}, N_z = 9$	1	full weak formulations three spatial resolutions 8 cores
Sect. 4.2.3/TC3	SE/SV 3D	$T_{end} = 17\text{s}, \Delta t = (0.001, 0.002)\text{s}, \Delta t_{save} = 0.002\text{s}$ $\Delta x = \Delta y = 0.05\text{m}, N_z = 9$	2	mild-slope approximation wavemaker stops at $t = 5.670\text{s}$ two time resolutions, 16 cores
Sect. 4.2.4/TC3b	SE/SV 3D	$T_{end} = 17\text{s}, \Delta t = (0.001, 0.002)\text{s}, \Delta t_{save} = 0.002\text{s}$ $\Delta x = \Delta y = 0.05\text{m}, N_z = 9$	2	full weak formulations wavemaker stops at $t = 5.670\text{s}$ two time resolutions, 16 cores
Sect. 4.4/TC4	SE/SV 2D	$T_{end} = 120\text{s}, \Delta t = 0.001\text{s}, \Delta t_{save} = 0.02\text{s}$ $\Delta x = 0.01\text{m}, N_z = 9$	-	wavemaker data, flat bottom $H_0 = 1.0\text{m}, L_x = 100\text{m}$ 16 cores

Table E.3: Details for simulations. SE=symplectic Euler. SV=Störmer-Verlet. All the test cases are run in Firedrake with default solver parameters.